Cross-linked chitosan/thiolated graphene quantum dots as a biocompatible polysaccharide towards aptamer immobilization

Arezoo Mirzaie, Mohammad Hasanzadeh, Abolghasem Jouyban

PII: S0141-8130(18)34973-0
DOI: https://doi.org/10.1016/j.ijbiomac.2018.11.139
Reference: BIOMAC 11016

To appear in: *International Journal of Biological Macromolecules*

Please cite this article as: Arezoo Mirzaie, Mohammad Hasanzadeh, Abolghasem Jouyban , Cross-linked chitosan/thiolated graphene quantum dots as a biocompatible polysaccharide towards aptamer immobilization. Biomac (2018), https://doi.org/10.1016/j.ijbiomac.2018.11.139

Cross-linked chitosan/ thiolated graphene quantum dots as a biocompatible polysaccharide towards aptamer immobilization

Arezoo Mirzaie [a], Mohammad Hasanzadeh [b*], Abolghasem Jouyban [c]

[a] Student Research Committee and Faculty of Pharmacy, Tabriz University of Medical Sciences, Tabriz, Iran.

[b] Drug Applied Research Center, Tabriz University of Medical Sciences, Tabriz, Iran.

[c] Pharmaceutical Analysis Research Center and Faculty of pharmacy, Tabriz University of Medical Sciences, Tabriz, Iran.

Corresponding Author
E-mail address: (*) hasanzadehm@tbzmed.ac.ir
Drug Applied Research Center, Tabriz University of Medical Sciences, Tabriz 51664, Iran.
Tel: +98(41) 33363311; Fax: +98(41)33363231

Abstract

Chitosan has a number of commercial and possible biomedical uses. Chitosan as a polysaccharide is a bioactive polymer with a variety of applications due to its functional properties such as antibacterial activity, non-toxicity, ease of modification, and biodegradability. In this work, cross-linked chitosan/thiolated graphene quantum dot as a biocompatible polysaccharide was modified by gold nanoparticle and used for immobilization of ractopamine (RAC) aptamer. A highly specific DNA-aptamer (5′-SH-AAAAAGTGCGGGC-3′), selected to RAC was immobilized onto thiolated graphene quantum dots (GQDs)-chitosan (CS) nanocomposite modified by gold nanostructures (Au NSs) and used for quantification of RAC. Different shapes of gold nanostructures with various sizes from zero-dimensional nanoparticles to spherical structures were prepared by one-step template-assistant green electrodeposition method. Fully electrochemical methodology was used to prepare a new transducer on a glassy carbon surface which provided a high surface area to immobilize a high amount of the aptamer. Therefore, a label free electrochemical (EC) apta-assay for ultrasensitive detection of RAC was developed. A special immobilization media consisting of Au NSs/GQDs-CS/Cysteamine (CysA) was utilized to improve conductivity and performance of the biosensor. The RAC aptamer was attached on the Au NSs of the composite membrane *via* Au-S bond. The fabrication process of the EC aptamer based assay was characterized by some electrochemical techniques. The peak currents obtained by differential pulse voltammetry decreased linearly with the increasing of RAC concentrations and the apta-assay responds approximately over a wide dynamic range of RAC concentration from 0.0044 fM to 19.55 µM. The low limit of quantification was 0.0044 fM.

Keyword; Biopolymer, chitosan; biocompatible nanocomposite, bioactive material, aptamer

1. Introduction

β-agonists were are well-known drugs for the treatment of pulmonary disease and asthma [1]. However, due to their potential roles in decreasing adipose tissue deposition and increasing protein accretion in livestock, they are illegally used as feed additives [2]. Because of good stability β-agonists can be easily deposited in human beings after meat consumption, and result in many serious health problems such as cardiovascular and central nervous diseases [3]. For their toxic side-effects, many countries have forbidden the use of β-agonists in stockbreeding [4]. Among them, ractopamine (RAC) is widely used in illegal applications and resulting in huge economic loss for export exchange transaction of edible meat products [5]. Based on the above facts, the routine monitoring of RAC abuse becomes exceedingly important for public health [6-10].

In the past few decades, electrochemical aptasensors based on the specificity of aptamer-target recognition have received particular attention because of their high sensitivity, low sample volume, short detection time, simple pretreatment procedure, low cost instrumentation, and automated detection [11, 12]. Different nanomaterials, including gold nanoparticles, carbon nanostructures, and quantum dots, have been used to modify detection signals to obtain highly sensitive electrochemical aptasensors [11-15]. However, many disadvantages, such as complicated procedures, high costs, and poor reproducibility and quantification, especially when complex samples are detected, have also been observed in the application of these nanomaterials [6-10]. Thus, simple aptasensors for ultrasensitive and convenient detection of drugs remain an urgent need.

Gold nanostructures (Au NSs) owing to the unique physical and chemical properties are useful to fabricate transducers of sensors and biosensors [16]. Au NSs are biocompatible and can be readily tuned by changing their size, morphology and surrounding chemical entity [17]. In addition, Au

NSs can offer multifunctional surfaces with a wide range of organic or biological macromolecules for selective binding and provide an excellent platform to fabricate other metallic nanostructures [18-20]. On the other hand, biomolecules such as aptamers can provide chelating groups for the interaction with Au NSs and act as signal amplification agents; this approach to generate nanomaterials is somewhat similar to the bio-mineralization behavior of many organisms in nature [18-20].

Fabrication of nanoparticles (NPs) and especially gold nanoparticles into graphene based materials (graphene nano-sheets, graphene oxide and graphene quantum dots (GQDs)) is a new method to enhance conductivity of these nanomaterials and is an excellent pathway for preparation of organic-inorganic nano-hybrid with high electrical properties which improved by incorporation of NPs [21-29]. Lately, application of graphene based materials modified by NPs/polymers and the use of these nanocomposites for bioanalytical aims was described in the literature [30]. One of important graphene based materials for this purpose is GQDs which could be an excellent candidate for electrodeposition and lead to preparation of a conductive interface for conjugation with NPs [31]. On other word, this matrix could be functionalized by NPs for better electrochemical performance.

In this work, considering benefits of the GQDs, Au NSs, CS, and Cysteamine (CysA) ,as thiolating species), we used these materials for the construction of a novel aptasensor to apply the synergy contributions on the enhancement of apt-assay characteristics. GQDs were modified with thiol (–SH) groups by binding the COOH groups of GQDs to the amine (NH_2) groups of CysA through amide bonds. The SH modified GQDs/CysA were used thereafter for electrochemical assembly of Au NSs.

The possibility of using the AuNSs/GQDs-CS-Cys A as a platform for the immobilization of aptamer and development of electrochemical aptasensors is examined. The superior performances encouraged us to explore the possible leading role played by the presence of AuNSs/GQDs-CS-Cys A on glassy carbon electrode (GCE) which could increase the surface area to interact with aptamer which is necessary for detection of RAC. Interestingly, various morphology of Au NSs can be providing different electrically conductive film towards amplifies Faradic currents of RAC. A novel low toxic and biocompatible interface of Au NSs/GQDs-CS-Cys A as using electrochemistry methods which show durable electroactivity toward the electrooxidation of RAC is prepared. To the best of our knowledge, the use of ordered Au NSs/GQDs-CS-CysA for immobilization of RAC aptamer and its application to fabrication of a label-free electrochemical aptasensor for the detection of RAC has not yet been reported.

2. Materials and methods

Chemicals and reagents

Potassium ferrocyanide $K_4Fe(CN)_6$, 1-ethyl-3-(3-dimethylaminopropyl) carbodiimide hydrochloride (EDC), N-hydroxysuccinimide (NHS), cysteamine hydrochloride, hydrogen tetrachloroaurate(III)hydrate ($HAuCl_4 \bullet 3H_2O$), were obtained from Sigma-Aldrich (Ontario, Canada). RAC were purchased from Sigma-Aldrich and reconstituted in Tris-HCl buffer 0.1 M. Aptamer was obtained from Boster Biological Technology Co. Ltd (Pleasan-ton, CA, USA), and the sequence were: 5′-SH-AAAAAGTGCGGGC-3′, 5′-SH-CCCCCCAGTGCGGGCCCCCC-3′, and 5′-SH- ACGCAGTGCGGGCGA-3′. Human plasma samples were obtained from the Iranian Blood/Plasma Transfusion Research Center (Tabriz, Iran).

Synthesis and Cytotoxicity of GQDs

GQDs was synthesized according to our previous report [32]. An easy bottom-up method was used for the preparation of GQDs. At first, GQDs were synthesized by pyrolyzing citric acid and dispersing the carbonized products into alkaline solutions. Briefly, 2 g of citric acid was put into a beaker and heated to 200 °C by a heating mantle until the citric acid changed to an orange liquid. Then, for preparing GQDs, 100 mL of 10 mg/mL NaOH solution was added into the orange homogenous liquid dropwise with continuous stirring. The obtained GQD solution was stable for at least one month at 4 °C.

To determine the effects of GQDs-induced toxicity NIH-3T3 and HepG2 cells were exposed to different concentrations of GQD (0, 10, 20, 50,100 and 200 ppm) for 24, 48 and 72 hour. Fig. S1 (see supporting information) represents the impact of GQDs treatment on the viability of cancerous cell line (HepG2) (A) and non-tumorigenic cell line (NIH-3T3) (B). Assessment of cell viability by MTT reduction cell viability test revealed that the increasing doses of GQD up to 200 ppm did not show any significant effects on cell death of both cell lines.

Also, the average lateral dimension of as-prepared GQDs was quite small compared with HepG2 cells. It has been reported that nano-sized GQDs could be internalized into cells faster compared with the micro-sized GO sheets. Moreover, as-prepared GQDs emitted intense green luminescence, so it might be a good candidate for fluorescent probes in cell imaging. As shown in Fig. S1 (C-D (see supporting information)), the laser scanning confocal microscopy image of the cells incubated (Fig. S1B and C (see supporting information)) with 200 ppm of GQDs was obviously brighter than that of the cells without GQDs treatment (Fig. S1A (see supporting information)), demonstrating that GQDs had internalized into the cells and mainly existed in cell membrane and cytoplasm, in agreement with the previous finding reported by Yuan's group. The results revealed that even at the low concentration of 50 ppm, the fluorescence of the cells was still

bright, which held great potential for bioimaging. In addition, GQDs could enter the cell cytoplasm, indicating another prospect of GQDs in drug delivery.

Synthesis of GQDs-CS

The nanocomposites of CS-GQDs were prepared as follows: CS solution (2 g L^{-1}) was prepared by dissolving CS in 0.1 M acetic acid, and then the yellow GQDs aqueous solution (2 g L^{-1}) was added into the CS solution under stirring. After 10 min of stirring, the mixture was adjust by addition of 10% (w/w) sodium hydroxide solution dropwise. The precipitate was washed with ultrapure water several times to remove the residual impurities, and the obtained CS-GQDs were freeze dried in a lyophilizer at -40 ◦C for 24 h.

Characterization of GQDs and GQDs-CS nanocomposite

For characterization of GQDs-CS, FT-IR, DLS, Zeta Potential analysis, DSC, XRD were used. The FT-IR spectra of GQDs-CS nanocomposites are shown in Fig. S2 (see supporting information). For GQDs, the two peaks at 1766 and 1716 cm^{-1} are assigned to the stretching vibrations of C=O from the −COOH groups. Two characteristic peaks centered at 1650 and 1604 cm^{-1} are observed at CS, which are attributed to the stretching vibrations of C=O from −NHCO− and the bending vibrations of N−H from $-NH_2$, respectively. The spectra of CS-GQDs nanocomposites exhibit a combination of characteristics similar to pure CS and GQDs, including the absorption peak located at 1708 cm^{-1} owing to the C=O stretching of GQDs, and the peak at 896 cm^{-1} due to the N−H out of plane bending vibrations from CS. Compared with pure CS and GQDs, the peaks at 1604 and 1766 cm^{-1} disappear at the spectra of CS-GQDs, suggesting the existence of strong electrostatic attraction between CS and GQDs. In addition, the C=O stretching of GQDs is downshifted from 1716 to 1708 cm^{-1}, which might be due to the formation of H-bondings within the nanocomposites.

Zeta potential analysis of GQDs and GQDs-CS was investigated to determine the surface charge and the stability of the synthesized material. As results revealed, the negative zeta potential value was changed to more negative potentials approving the attachment of CS where the negative charge have a major effect in stability of GQDs-CS. Particle size of materials is normally observed by DLS. DLS analyses of GQDs and GQDs-CS show an increase in the particle size of the GQDs-CS which confirmed by zeta potential analysis.

Finally, these results indicating that the GQDs-CS nanocomposites prepared via simple and convenient assembly exhibit a well-dispersed status due to the strong interactions, electrostatic attraction and H-bindings, between CS and GQDs [32].

Aptasensor assembly

Physical and electrochemical cleaning of the electrode

First, the physically cleaning of GCE was done in three steps: polishing with alumina powder on polishing pad, sonication in ethanol and then in distillated water, and finally drying with nitrogen stream.

For pre-treatment of GCE, the electrode was washed with 0.1 M nitric acid/ hydrochloridric acid solution and 1:1 of distillated water/acetone, respectively. Then the electrode was polished on the polishing pad with 0.2 μm alumina slurry. For more cleaning of the electrode surface, the GCE was soaked in 0.5 M H_2SO_4 and cycled between -0.2 to 0.8 V for 30 times with CV technique until reaching repetitive cycles.

Electrodeposion of GQDs-CS on the surface of GCE

Fig. 1 shows the electrochemical deposition of GQDs-CS on the surface of GCE. The procedure for electrodeposition of GQDs-CS on the GCE surface was not previously reported in the literature. Herein, the electrochemical deposition of GQDs-CS on GCE is considered. In this work, the GCE

was placed in the cell containing 10 mL of GQDs-CS and subsequently, electrochemical deposition of GQDs-CS on the electrode surface was conducted through CV with 30 consecutive cycles in the potential range of 0 to 1 V *vs.* Ag/AgCl with sweep rate of 100 mV/s (Fig. 4). For this purpose, GQDs-CS/GCE was prepared by CV technique.

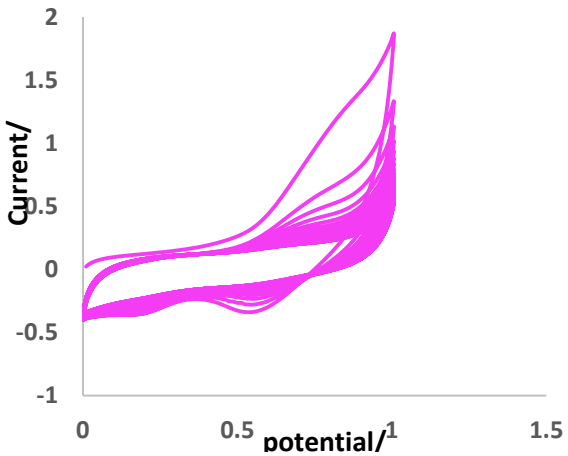

Figure 1: Electrochemical deposition of GQDs-CS on the surface of GCE. The cyclic voltammogram depicts grasignal growth of GQDs-CS after 30 successive cycles in the range of 0 to +1 V with scan rate of 0.1 V/s.

In acidic media, CS can be protonated to its cationic state via the protonation of the $-NH_2$ groups at the C-2 position of the D-glucopyranose repeating unit; [33, 34] meanwhile, the surface of GQDs is highly negatively charged when dispersed in water as the result of ionization of oxygen-containing functional groups (mainly−COOH) on the GQDs, which is favor of their combination with positively charged CS. Further evidence comes from the measurement of zeta potentials, CS with NH_3^+ groups is positively charged (+65 mV) and GQDs are negatively charged (−10 mV). The $-NH_3^+$ groups on CS contribute to the electrostatic attraction with predominant −COO− groups of GQDs. On the other hand, there also exist extensive H-bondings between$-CH_2OH$ groups of CS and −OH groups on the surface of GQDs. Both electrostatic attraction and H-

bondings induce interfacial adhesion of CS and GQDs and result in the formation of homogeneous nanocomposites of CS-GQDs (Scheme 1).

GQDs have good water solubility in a wide pH range, which is attributed to the plenty of hydrophilic groups existing on GQDs [35]. Also, pure CS would be dissolved in aqueous solution at pH below 6.3 due to the protonation of its $-NH_2$ groups. [36, 37] So in this work, both GQDs and pure CS can not be used to modify GCE individually. However, the strong electrostatic interactions between positively charged CS and negatively charged GQDs result in the aggregation and subsequent preparation of the CS-GQDs, leading to stable existence of the nanocomposites over a wide pH range (4.5~11.0). This phenomenon is similar to previously reported cationic CS-based polyelectrolyte complexes with anionic κ- carrageenan [38], carboxymethyl cellulose [39], and poly(2-acryloylamido-2-methylpropanesulfonic acid) [40]. It should be pointed out extreme acidity (pH < 4.5) or alkalinity (pH > 11.0) can cause the dissociation of the CS-GQDs owing to the blocked Coulomb forces between the two components and the destroyed condensed state of the complex by the increased local charge density. Anyway, the enhanced stability of the CS-GQDs over the pH range from 4.5 to 11.0 compared with pure CS and GQDs makes the nanocomposites an ideal electrode modifier to be used in the acetate buffer of pH 5.5.

Thiolation of GQDs-CS nanocomposite towards electrodeposition of Au NSs

The GQDs/GCE were further modified with thiol (–SH) groups by binding the COOH groups of GQDs to the amine (NH_2) groups of CysA through amide bonds. The SH modified electrode (CysA/GQDs-CS/GCE) was used thereafter for electrochemical assembly of Au NSs. For this purpose, a fully electrochemical method for preparation of the substrate were used. The CysA/GQDs/GCE was placed in the solution contained 10 mM ($HAuCl_4$), H_2SO_4 (100 mM), and

arginine (Arg) (20 mM). Electrodeposition was performed at 0-1.5 V V for 500 s. Then CysA/Au NSs/GQDs-CS/GCE electrode was then rinsed thoroughly with distilled water.

Previous studies revealed dependency of deposition potential on the size and morphology of generated Au NSs. Shi et al. demonstrated that the crystal density of generated Au NSs increases by shifting toward negative electrodeposition potentials from -0.3 to 0.3 V on ITO electrode, because of increase in nucleation rate when over saturation occurs at higher overpotentials [41]. Electrodeposition has an important role on the morphology, distribution and thickness of Au NSs on the surface of GCE. For electrodeposition of Au NSs on the surface of GCE, the electrodeposition of metallic gold ions by chronoamperometry technique was carried out in the cell containing solution of 10 mM ($HAuCl_4$), H_2SO_4 (100 mM), and arginine (Arg) (20 mM). Au NSs was electrodeposited on the GCE modified by CysA/GQD, and CS. Briefly, 10 mL of above mentioned solution was transferred to electrochemical cell. In the present study, the electrodeposition was controlled by the potential of chronoamperometry (E=0, 0.2, 0.5, 0.7, 1, and 1.5 V *vs.* Ag/AgCl). Therefore, the electrodeposition potential was set and time duration of the chronoamperometry was adjusted at 500 s. For the fabrication mechanism of Au NSs, it can be mentioned that gold atoms or clusters are initially and rapidly formed, followed by promoted nucleation. The Arg adsorption process causes to formation of AuNSs-stable Arg layer in which Arg is involved to the surface *via* the zwitterions functional group, and its positively charged functional group tends outward into the solution. Therefore, $AuCl_4^-$ ion was electrostatically absorbed on the surface of Arg and cause to preferential growth of Au by the diffusion-limited aggregation mechanism (Fig. 2).

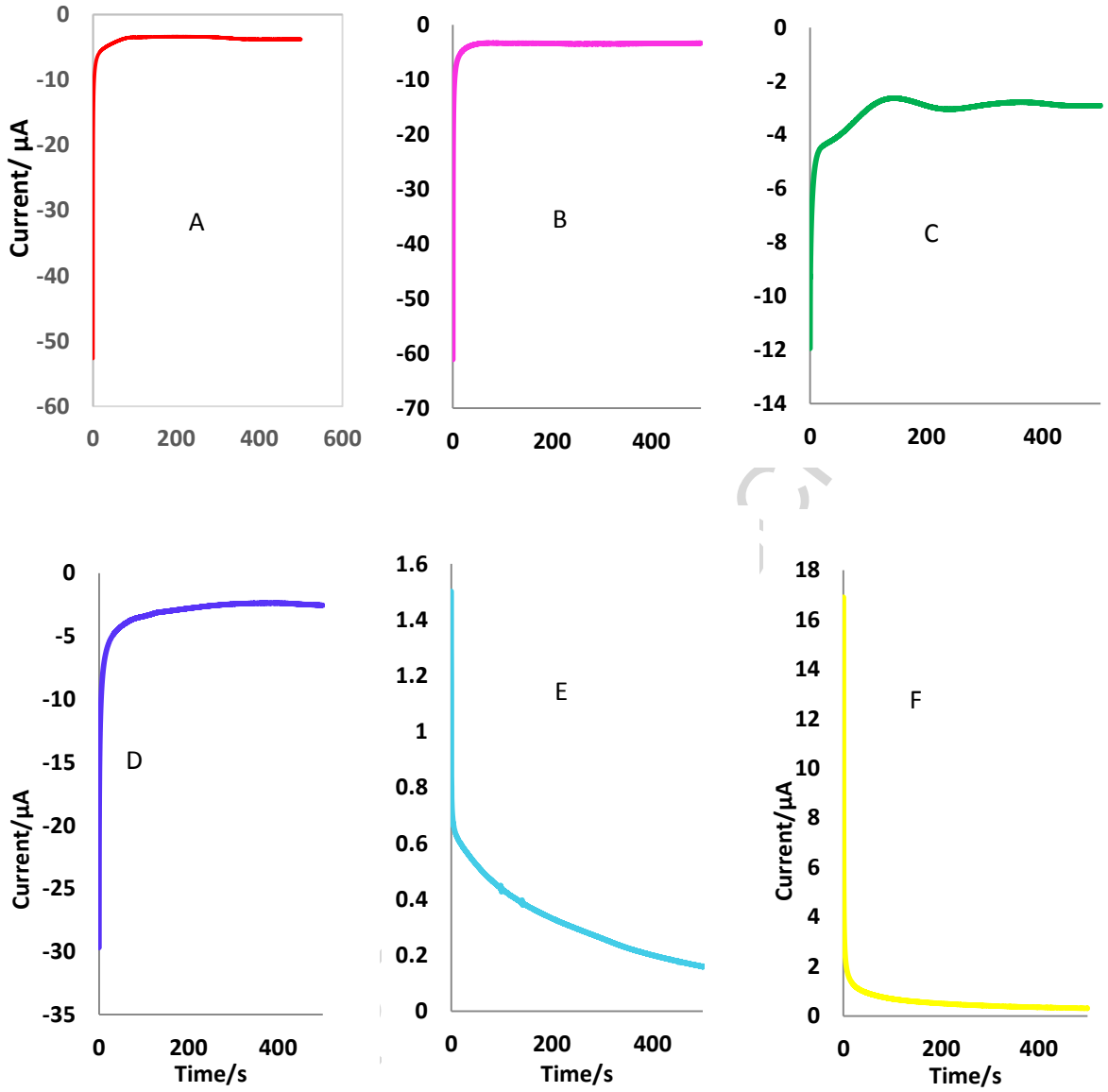

Fig. 2. Chronoamperograms of GCE modified CysA-GQD-CS in the solution contain 10 mM $HAuCl_4$ + 20 mM Arg + 100 mM H_2SO_4 in different potentials (**A**) E=0.0 V, **B**) 0.2 V, **C**) 0.5 V, **D**) 0.7v, **E**) 1.0 V , and **F**) 1.5V, t=500 s.

Affinity of amino acid to bind with gold surface has been investigated both theoretically [42-45] and experimentally [44, 46, 47]. Amino acids have also been employed as soft templates for the synthesis of gold nanostructures [48]. Gold has also affinity to amine functional group [44, 47, 49,

50]. During the electrodeposition of gold, nucleation, adsorption (of additives), branching, and growth are the dominant steps. From these steps, kinetics of the growth step is slow and controls the total process. At the early stage of the electrodeposition, $AuCl_4^-$ was quickly reduced to gold atoms, followed by distribution of gold nuclei at the surface. If an additive (Arg in this case) is present in the solution, it is rapidly and selectively adsorbed (mainly *via* hydroxyl functional groups) on the specific planes of gold crystal. This adsorption prevents the newly generated gold atoms to be aggregated with the previously deposited ones. On the other hand, the additives act as shape directing agents and depending on their chemical structures facilitate the gold crystal growth at a specific directions. If the electrodeposition is performed at low potentials, the hydrogen co-evolution process would be the main shape-directing agent.

Regarding the real surface areas, gold nanostructure with petal shape and small tentacle had the highest and gold nanoparticles with spherical structure had the lowest real surface areas. There was a wide range of roughness factor, and different shapes of gold provide huge different surface areas. Electrochemical activity of the gold structures was also different depending on the shape and size from both kinetic and thermodynamic points of view. The different peak currents for the redox peaks of the analytes (RAC) can be related to the active surface areas of the Au NSs and different shapes and sizes causing the reactions to occur at different potentials. It depended on both the entity of the analyte and the shape and size of the Au NSs; the best Au NS can be selected for aptamer immoblization.

Immobilization of aptamer

After preparing the substrate containing Au NSs /CysA- GQDs-CS/ with different morphologies, the electrodes were gently rinsed and after drying, the immobilization of aptamer on the surface of electrodes was performed. For this purpose, 12 nM primary aptamer (5′-SH-

AAAAAGTGCGGGC-3′) was diluted in 500 µL of (Tric-HCl buffer). The GCE modified by different shapes of Au NSs /GQDs-CS/CysA was incubated with 10 µL of primary aptamer for 2 h at -4 ^{o}C. Then the blocking reagent 2-mercapto ethanol (2-MCE) was added to the surface of Apt/Au NSs /GQDs-CS/CysA-GCE to reduce non-specific adsorption for 1 h. According to previous studies, in the fabrication of aptasensors, one of the most popularly used electrode materials is gold nanoparticles with different morphologies, upon which thiolated aptamer can be immobilized via strong Au-S linkages [51-53]. The modification of DNA or RNA with a terminal thiol is straightforward: simple phosphoramidite chemistry on the DNA/RNA synthesizer suffices. The modification of Au NSs surfaces with the thiolated oligonucleotide strands is readily accomplished by dipping a cleaned Au slide into the deposition solution to form an aptamer layer. Although the initial adsorption of thiolated DNA strands onto Au NSs occurs within minutes, it is necessary to allow the reaction to continue for up to 2 h to ensure a homogenous surface. The resulting surface is usually subjected to a passivation step (*i.e.*, treated with 2-mercapto-ethanol solution) to minimize non-specifically bound oligonucleotide strands. Finally, the electrodes were rinsed with deionized water to remove excess aptamer and used for further study. The schematic representation of the attaching event is described in Scheme 1.

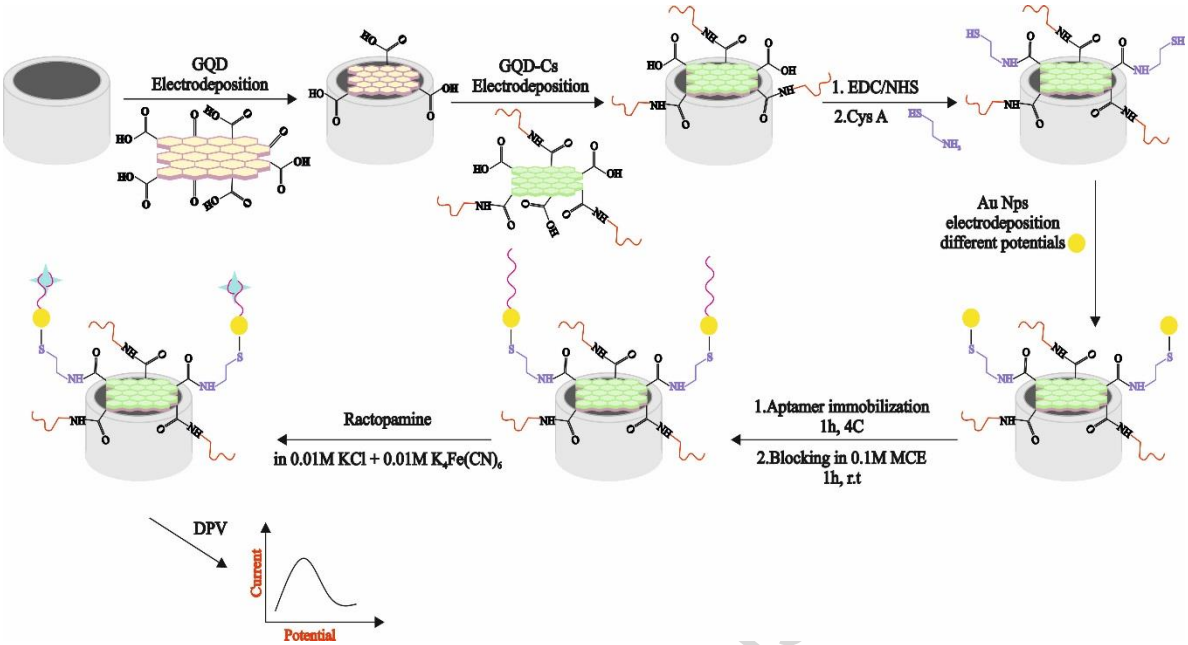

Scheme 1: Schematic representation of aptasensor preparation

Apparatus

Electrochemical measurements were conducted using conventional three-electrode cell (from Metrohm), containing Ag/AgCl-saturated KCl as reference, a platinum wire as counter electrodes and GCE as working electrode (GCE) (d=2mm) which powered by an electrochemical system comprising of Palmsens system with PS4.F1.05 (Palm instruments, Utrecht, The Netherlands). The system was run on a PC using PSTrance 5.3 software.

The surface morphology of electrode surface was characterized by high-resolution field emission scanning electron microscope (FE-SEM, Hitachi-SU8020, Czech) with an operating voltage of 3 kV, and chemical compositions of the Au NSs were analysed by an energy dispersive X-ray spectroscopy (EDS) coupled with the FE-SEM equipment. Fourier transform infrared (FTIR) spectra were recorded on a Shimadzu model FTIR prestige 21 spectrophotometer (Tokyo, Japan) using KBr discs. X-ray diffraction (XRD) patterns were recorded on a Siemens D 5000 X-Ray

diffractometer (Texas, USA) with a Cu Kα anode (λ = 1.54 A°) operating at 40 kV and 30 mA. The diffraction patterns were collected at 25 °C and over an angular range of 3.0 to 10 and 10 to 70° with a dwell time of 12 s per increment and step size of 0.05° per step. The particle size distribution and zeta potential values were measured by Malvern particle size analyzer (Malvern, UK). Differential scanning calorimetry (DSC) diagram was recorded by a model Jade DSC, PerkinElmer (Aachen, Germany).

3. Results and discussion

Field emission scanning electron microscopy (FE-SEM) and energy dispersive X-ray spectroscopy (EDS)

After electrochemical deposition of Au NSs on the surface of GQDs-CS-CysA-GCE, the electrodes were employed for taking FE-SEM images for monitoring the distribution of Au NSs and morphology of the engineered electrode surface. The FE-SEM images of the engineered electrodes were shown in Fig. 3 (A-C) at different magnitudes. As can be seen, the surface of unmodified GCE (Fig. 3A) is smooth although the FE-SEM image of the GQDs (Fig. 3B) displays a number of aggregated bright dots positioned over the entire surface particularly at the wrinkle sites. The results were confirmed by TEM images of GQDs on the surface of GCE (inset of Fig. 3B).

According to Fig. 3, it can be seen the white dots are related to the Au NSs attached on the GQDs-Cs-Cys A; meanwhile the figure shows that some of Au NSs have been aggregated. The overall shape and size of Au NSs were found to be about petal, cubic and spherical with 25, 50, 30 nm, in the electrodeposition potentials (E= 0-1.5 v) respectively. For more confirmation, the chemical composition of the Au NSs-GQDs-Cs-Cys A-GCE was measured by point EDS. The EDS result

has been presented in (Fig. S3 (see supporting information). The EDS graph shows that the nanocomposite consists of only Au and C, O, N, S elements. It also confirms the attachment of Au NS on the GQDs-Cs-Cys A.

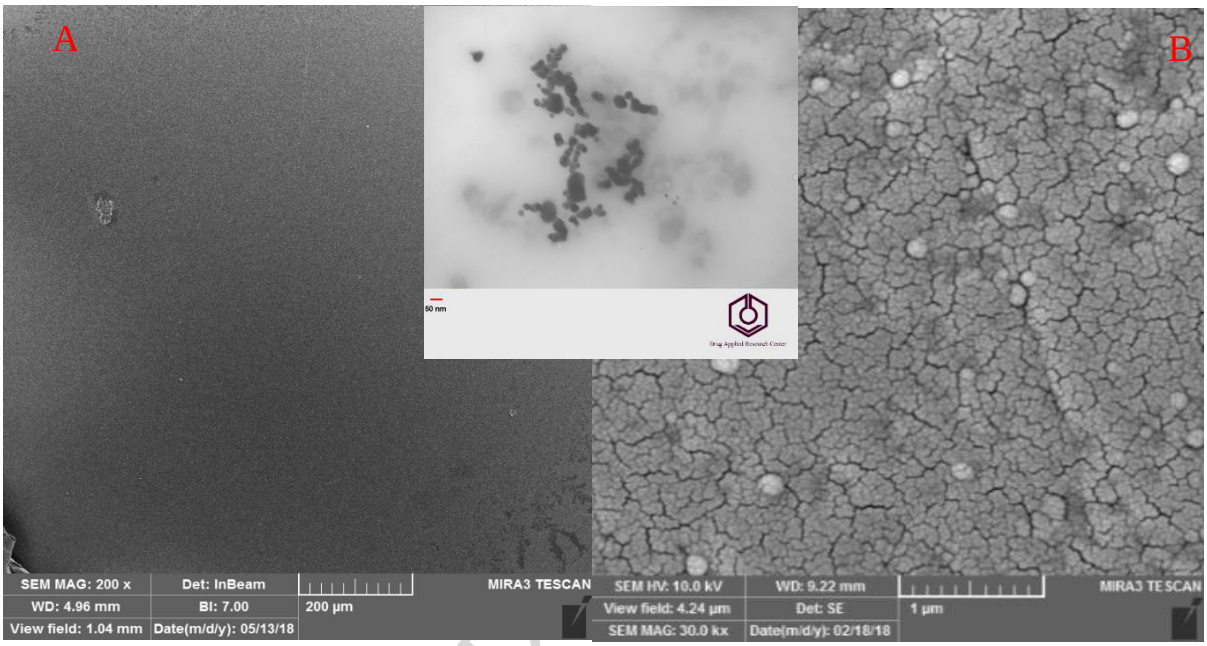

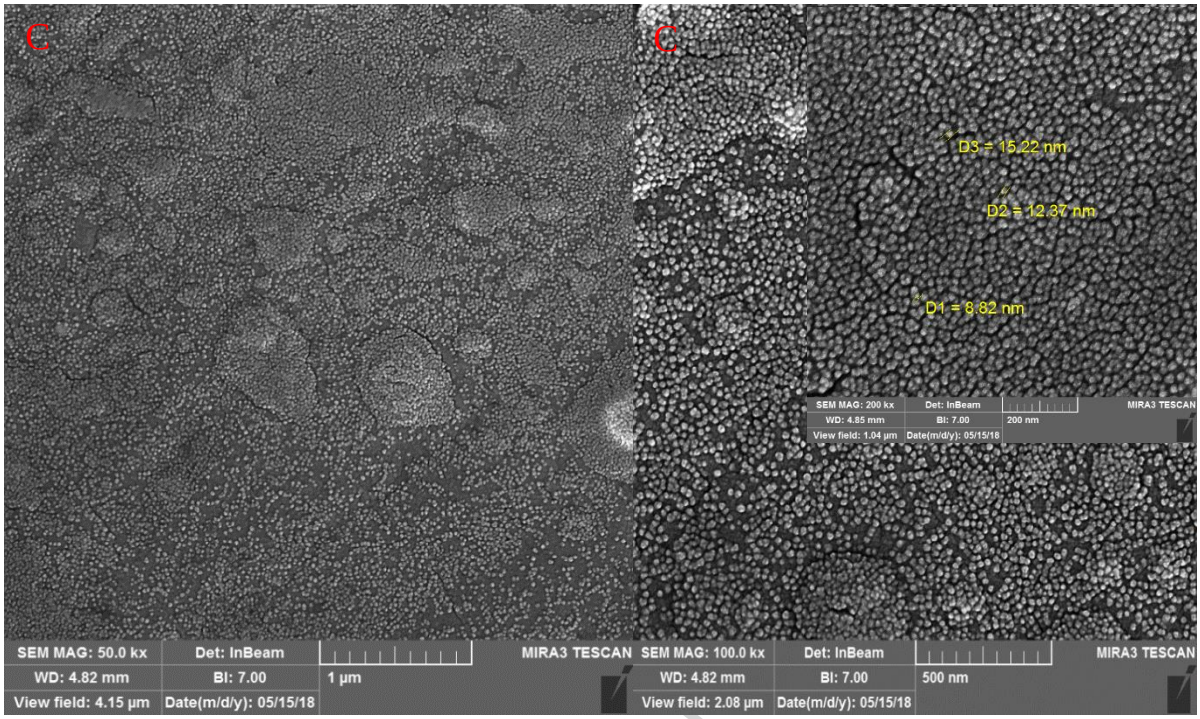
C
SEM MAG: 50.0 kx
Det: InBeam
MIRA3 TESCAN
WD: 4.82 mm
BI: 7.00
1 µm
View field: 4.15 µm
Date(m/d/y): 05/15/18
C
D3 = 15.22 nm
D2 = 12.87 nm
D1 = 8.82 nm
SEM MAG: 200 kx
Det: InBeam
MIRA3 TESCAN
WD: 4.85 mm
BI: 7.00
200 nm
View field: 1.04 µm
Date(m/d/y): 05/15/18
SEM MAG: 100.0 kx
Det: InBeam
MIRA3 TESCAN
WD: 4.82 mm
BI: 7.00
500 nm
View field: 2.08 µm
Date(m/d/y): 05/15/18

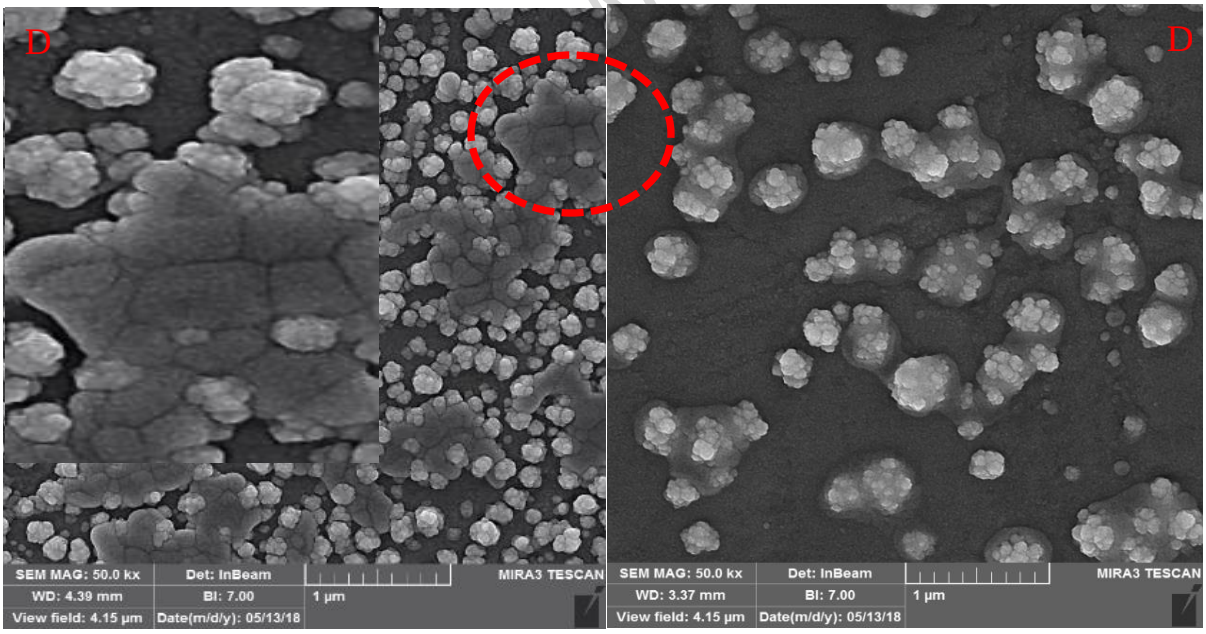
D
SEM MAG: 50.0 kx
Det: InBeam
MIRA3 TESCAN
WD: 4.39 mm
BI: 7.00
1 µm
View field: 4.15 µm
Date(m/d/y): 05/13/18
D
SEM MAG: 50.0 kx
Det: InBeam
MIRA3 TESCAN
WD: 3.37 mm
BI: 7.00
1 µm
View field: 4.15 µm
Date(m/d/y): 05/13/18

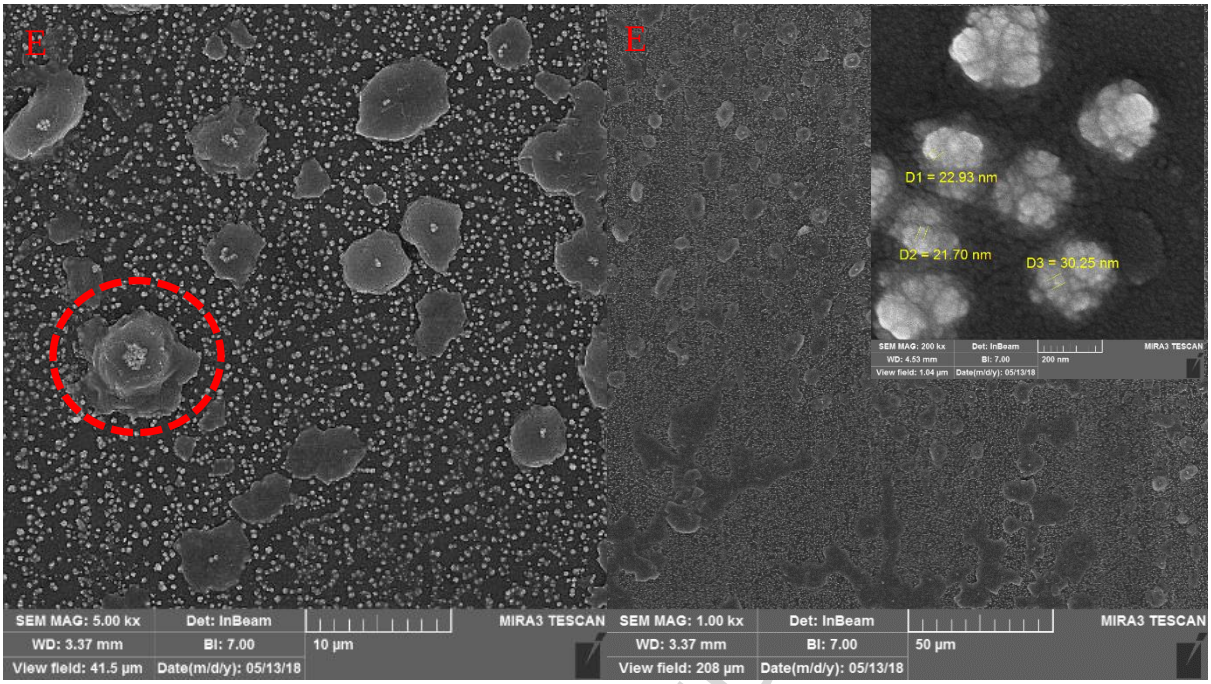
E
SEM MAG: 5.00 kx
Det: InBeam
MIRA3 TESCAN
WD: 3.37 mm
BI: 7.00
10 µm
View field: 41.5 µm
Date(m/d/y): 05/13/18
E
D1 = 22.93 nm
D2 = 21.70 nm
D3 = 30.25 nm
SEM MAG: 1.00 kx
Det: InBeam
MIRA3 TESCAN
WD: 3.37 mm
BI: 7.00
50 µm
View field: 208 µm
Date(m/d/y): 05/13/18

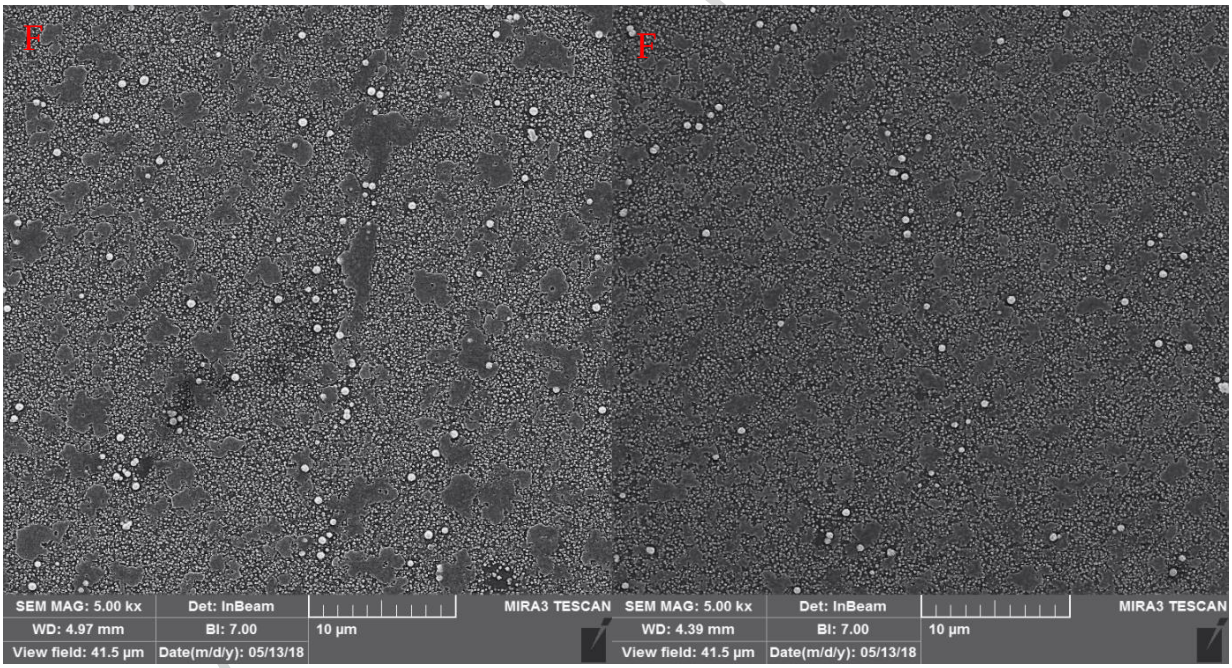
F
SEM MAG: 5.00 kx
Det: InBeam
MIRA3 TESCAN
WD: 4.97 mm
BI: 7.00
10 µm
View field: 41.5 µm
Date(m/d/y): 05/13/18
F
SEM MAG: 5.00 kx
Det: InBeam
MIRA3 TESCAN
WD: 4.39 mm
BI: 7.00
10 µm
View field: 41.5 µm
Date(m/d/y): 05/13/18

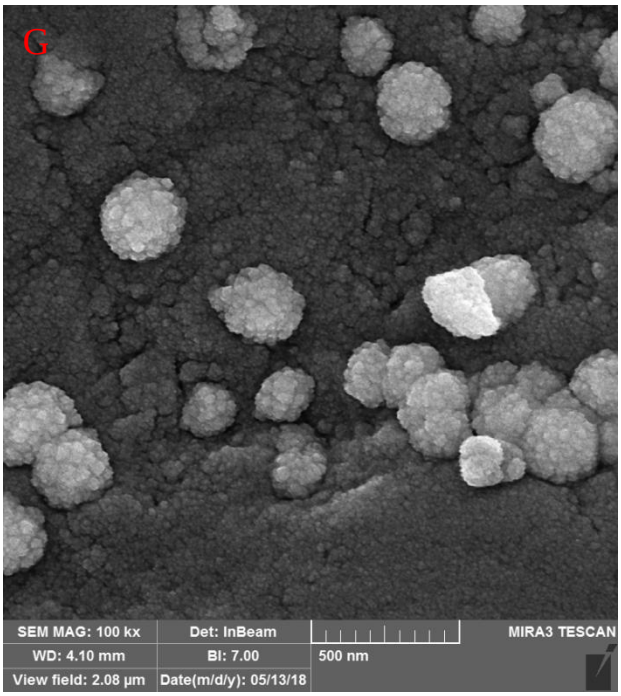
G
SEM MAG: 100 kx
Det: InBeam
MIRA3 TESCAN
WD: 4.10 mm
BI: 7.00
500 nm
View field: 2.08 µm
Date(m/d/y): 05/13/18

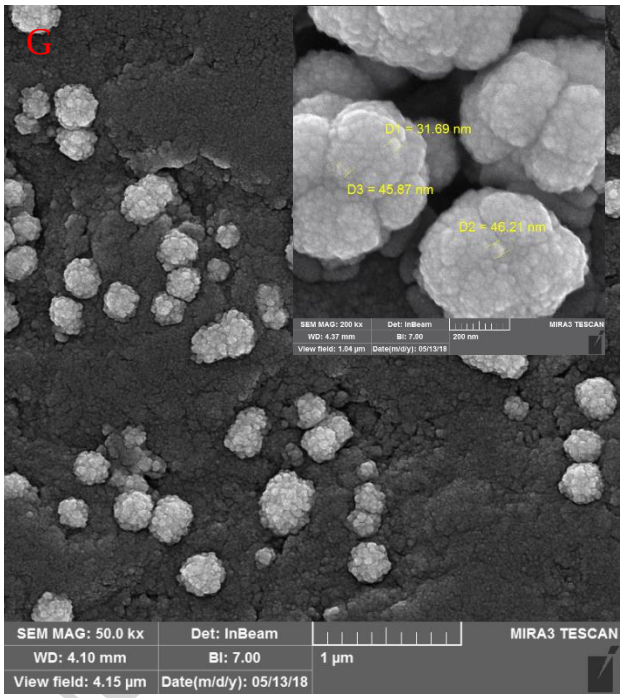
G
D1 = 31.69 nm
D3 = 45.87 nm
D2 = 46.21 nm
SEM MAG: 50.0 kx
Det: InBeam
MIRA3 TESCAN
WD: 4.10 mm
BI: 7.00
1 µm
View field: 4.15 µm
Date(m/d/y): 05/13/18

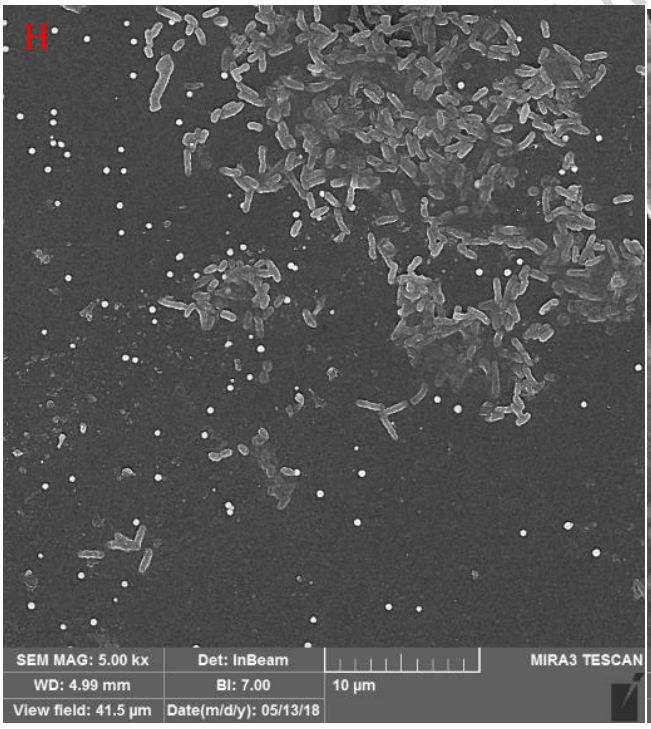
H
SEM MAG: 5.00 kx
Det: InBeam
MIRA3 TESCAN
WD: 4.99 mm
BI: 7.00
10 µm
View field: 41.5 µm
Date(m/d/y): 05/13/18

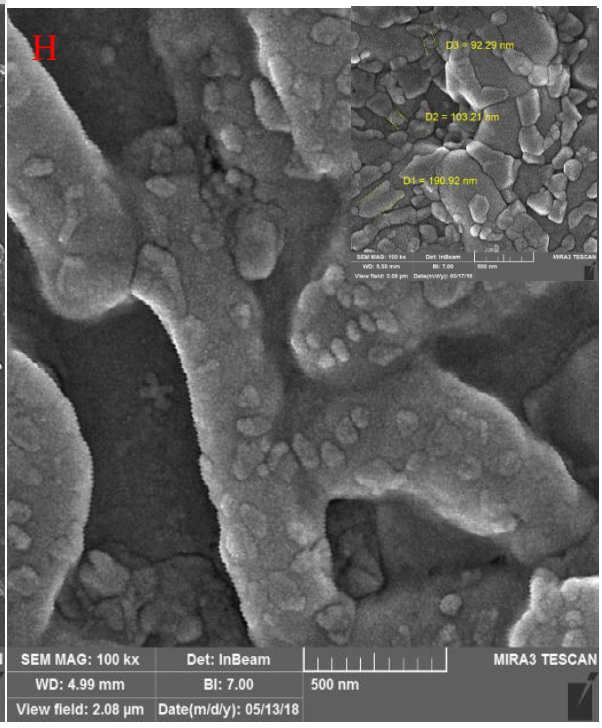
H
D3 = 92.29 nm
D2 = 103.21 nm
D1 = 190.92 nm
SEM MAG: 100 kx
Det: InBeam
MIRA3 TESCAN
WD: 4.99 mm
BI: 7.00
500 nm
View field: 2.08 µm
Date(m/d/y): 05/13/18

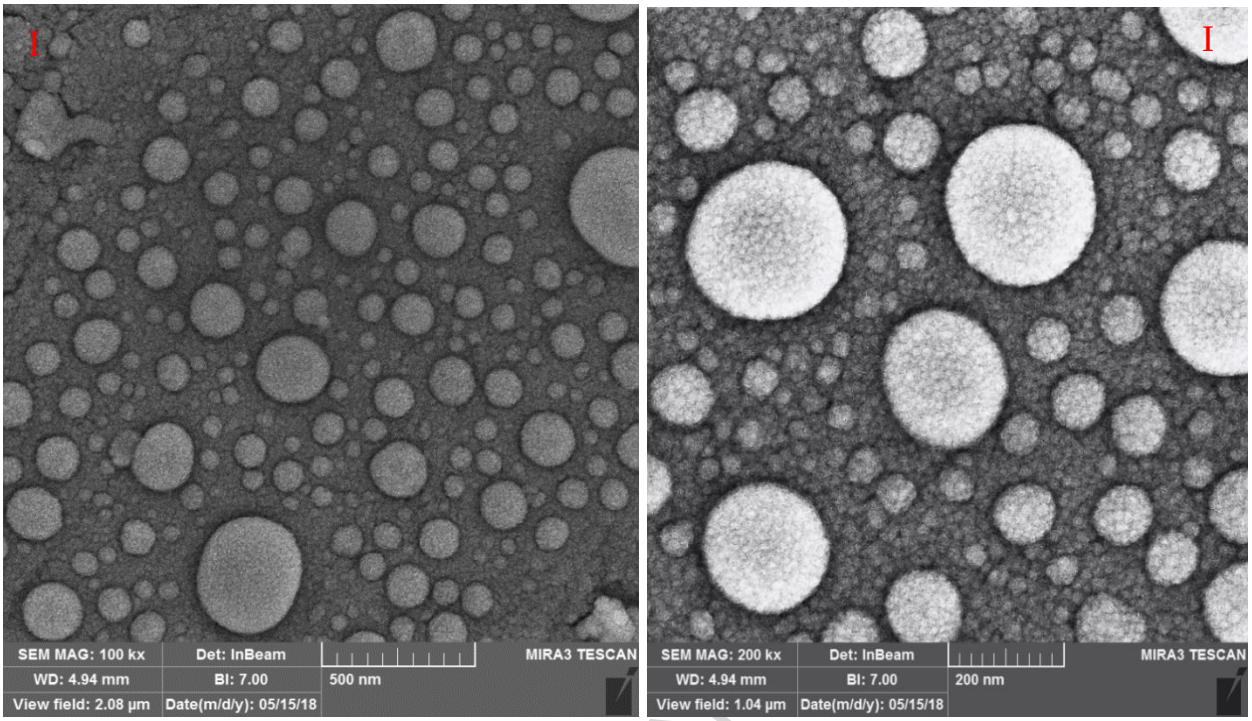

Figure 3. FE-SEM images of the GCE (**A**) and GQDs-CS/GCE **(B**), GQDs-CS-Cys A (**C**), (**D-I**) Au NSs- Cys A/GQDs-Cs in different deposition potentials (E=0.0, 0.2, 0.5, 0.7, 1, and 1.5V), respectively. Inset of **A**) TEM image.

The FE-SEM images of Au NSs/GQDs-CS-CysA/GCE show spherical/cubic/rod/flower like particles with uniform structure (Fig. 3), revealing that the Au NSs were indeed assembled onto the surface of thiolated GQDs-CS. Interestingly, more dispersed and less aggregated Au NSs are seen upon the electrostatic interactions of GQDs-CS-CysA with the Au NSs. Possibly the binding of positively charged GQDs-CS-CysA to the negatively charged Au NSs reduced the aggregation of the NSs through steric hindrance, although the loss of some Au NSs from the GQDs-CS-CysA surface cannot be eliminated.

All of the above results were summurized in the Scheme 2.

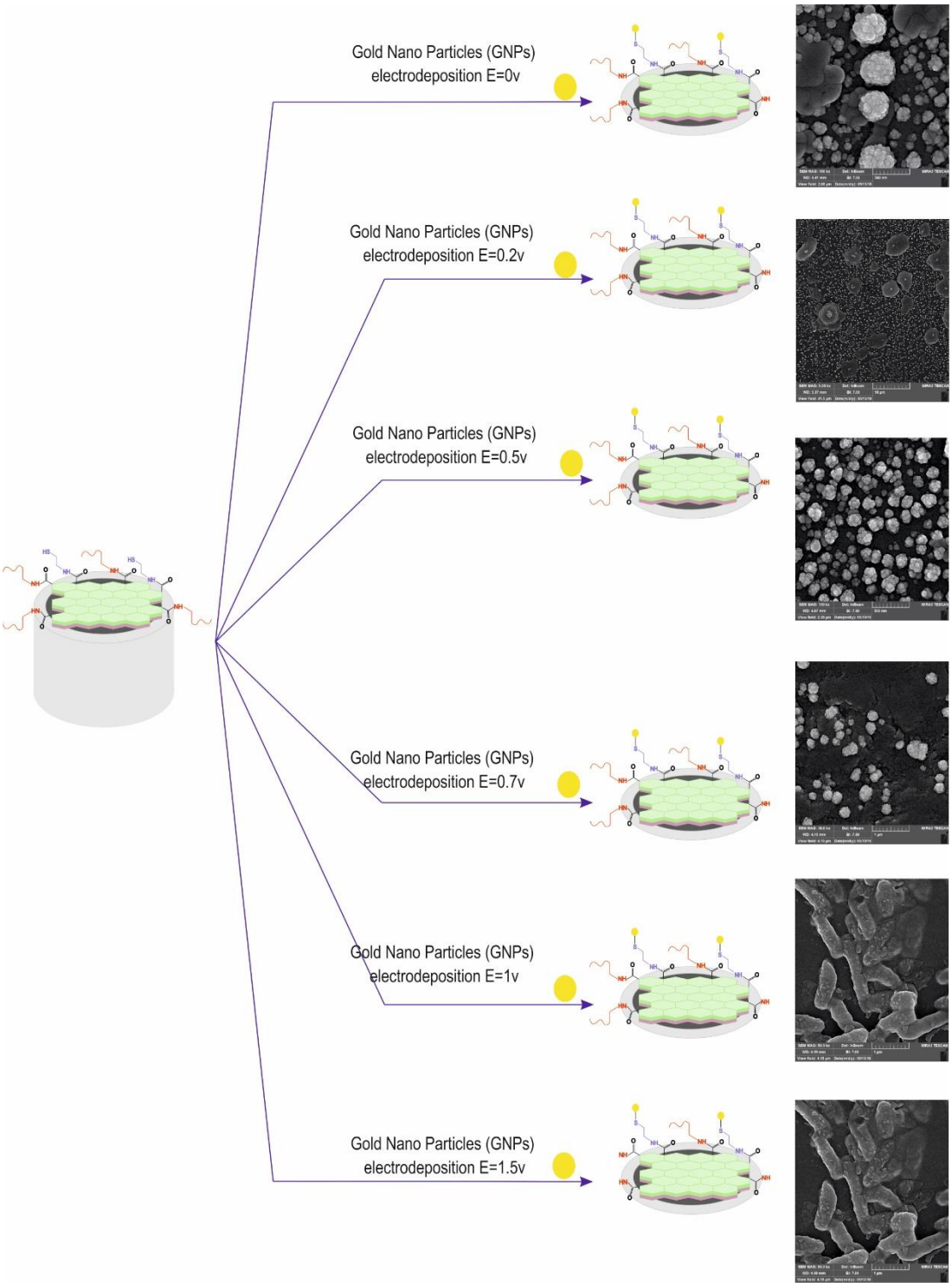

Scheme 2: The effect of different modification steps of the aptasensor.

Electrochemical characterization of electrode surface modification

CV technique has been proven as one of the common tools for probing the features of surface modified electrodes. In this work, CV was carried out to study the modification of the electrode surface. To understand the electrochemical properties of modified electrode, CVs were recorded with $[Fe(CN)_6]^{3-/4-}$ as a supporting electrolyte. As shown in Fig. S4 (see supporting information), a couple of well-defined redox peaks could be observed at the modified electrode.

The aptasensor fabrication steps were also monitored by recording CVs, SWVs, and DPVs from an equimolar solution of $[Fe(CN)_6]^{3-/4-}$. CVs of the $[Fe(CN)_6]^{3-/4-}$ containing 0.1 M KCl solution at the GCE, GQDs-CS- GCE, CysA-Cs/GCE surface showed a peak potential at about 0.6 V (Fig. S4 (see supporting information)). After the assembly of Au NSs onto the CysA/GQDs/GCE surface, the peak potential shifted to -0.034 V and the peak current increased. Upon aptamer binding onto the Au NP surface, the peak current decreased which confirmed the successfully immobilization of aptamer on to Au NSs-CysA/GQDs-CS/GCE. Finally, further decrease of the I_p was observed following the MCH blocking of the Apt-Au NSs-CysA-GQDs-CS-GCE surface by covering the remaining exposed Au NSs and GQDs surfaces.

In the case of bare GCE, the peak potential difference (ΔE_p) of 96.2 mV ($I_{pc}/I_{pa} \approx 1$) was observed, which indicates a quasi-reversible redox reaction. Also, the peak current is 4.69 µA. Whereas in the case of Au NSs modified CysA-GQDs-CS-GCE, the anodic peak current increased considerably (I_p=5.09 µA), which indicates the high redox reaction of $K_3Fe(CN)_6]^{3-/4-}$ at the interface due to the thin layer of Au NSs formed at the Cys-GQDs-CS-GCE. On the other hand, this is attributed to the reduction of Au(I) to Au(0) at the electrode surface. After the immobilization with aptamer, a small shift in the oxidation peak toward negative potential is obtained with a slight decrement in the redox current, indicating the proper binding of aptamer on

Au NSs modified electrode. The decrease in peak current at the electrode interface is attributed to the proper binding of aptamer with Au NSs through the 5′ end SH groups present in the aptamer with gold nano-cluster formation, which in turn enhance the electron transfer and thus electrochemical activity of the final modified electrode Apt/Au NSs-CysA-GQDs-CS-GCE was decreased. The changes in the current response during each stage of modification of GCE reveals the formation of AuNSs thin film and the proper immobilization of aptamer. Following aptamer incubation, the electrodes were thoroughly rinsed in Tric-HCl (pH 7.4) to remove the unbound aptamer. Then 2-MCE solution (0.1 M) was added to the modified surface and left for 1 h to block the free sites of Apt/AuNSs-CysA-GQDs-CS-GCE surfaces to minimize the non-specific binding. Finally, further decrease of the I_p was observed following the 2-ME blocking of the Au NSs surface by covering the remaining exposed Au NSs surfaces. The aptasensor were then directly subjected to apta-assay reaction with RAC or to electrochemical measurements.

Also, Fig. S4 (see supporting information) shows CVs of different modification steps. According to obtained results, in the absence of RAC, the peak current is 3.77 by CV technique. But, in the presence of RAC the I_p was decreased to 3.44 which confirmed the interaction of aptamer with target analyte. Therefore, it is obvious that this aptasensor has a suitable ability to detect RAC. Similar results were obtained by DPV technique (Fig. S4 (see supporting information)). All of obtained results were summarized in the Fig. 4 which shows histogram of peak current in different modification steps.

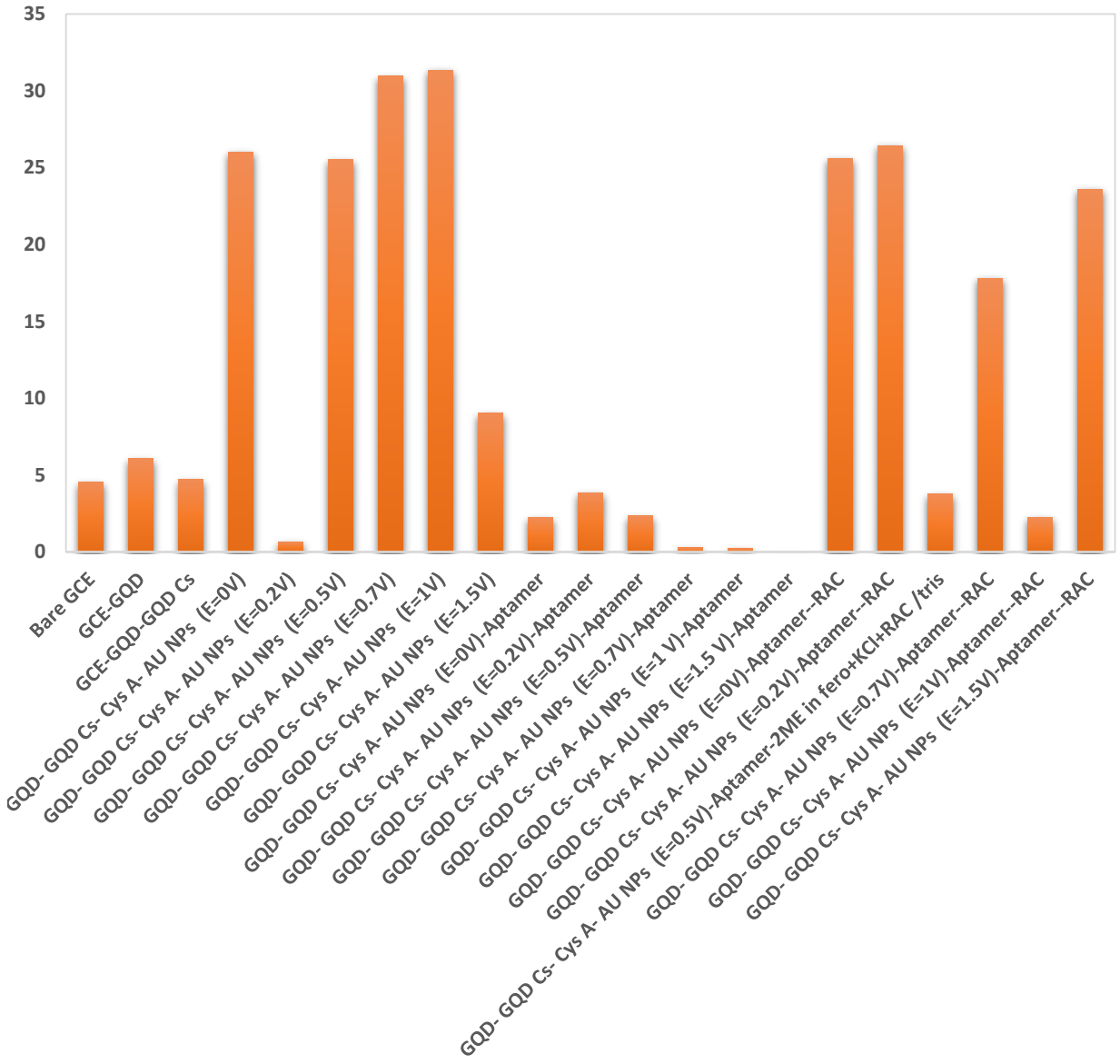

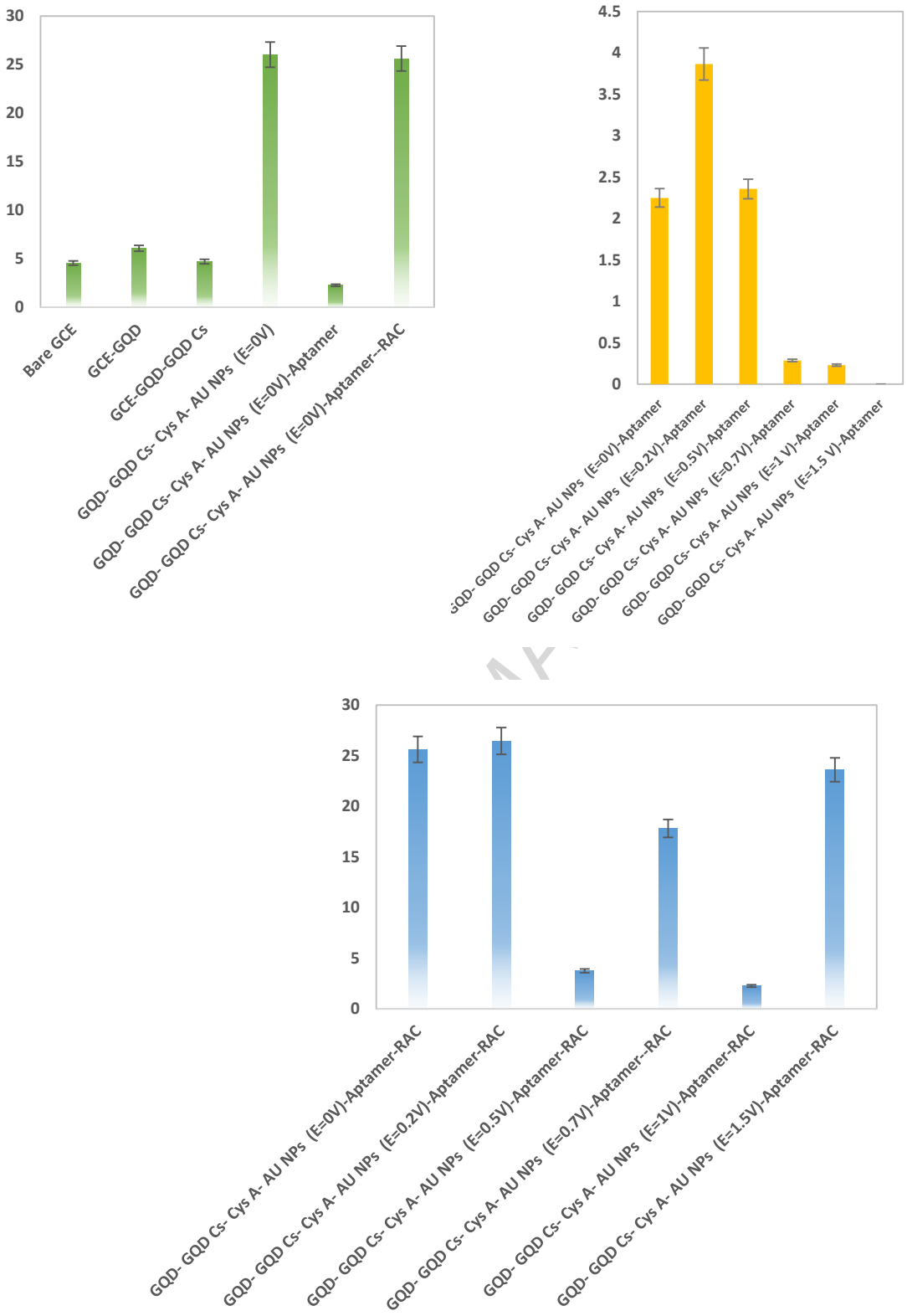

Fig. 4: Histograms of the different modification steps.

According to obtained results, in the presence of RAC, it was observed that the anodic peak current increased to about 20 µA. This implies that most of the electrode surface is covered by aptamer. Also, this observation demonstrates that the covalent immobilization of aptamer has been achieved successfully. The results indicate that a sensing interface is effectively constructed and successfully applied for the detection of RAC. This suggests that in the presence of RAC, due to the formation of complex RAC/aptamer functionalized AuNSs on the surface of the electrode, the aptamer folds into a RAC-binding three-way junction and hence, AuNSs with negative charge at the end of the aptamer move to a location near the electrode surface. Therefore it can be said that the existence of a greater negative charge (negative charges both of the aptamer phosphate group and Au NSs) led to a greater repulsion of the electrode surface with $[Fe(CN)_6]^{4-/3-}$ anions and the interfacial charge transfer was increased.

During the determination of RAC using the developed aptasensors based on one kind of gold nanostructures modified GCE, the variations of electrochemical performances were characterized through, DPV. Among them, DPV has been regarded as a sensitive method to probe the electron transfer of an interface between the electrolyte solution and modified electrode. In the DPV, the peaks observed at E≈0.3 V *vs.* Ag/AgCl corresponds to the electron transfer limiting process using GCE modified by Au NSs with petal structure. Also, the peak current was 2.8 µA because changes of the peak currents were as I_p Au NSs-petal> I_p Au NSs-cubic> I_p Au NSs- spherical. When Glassy carbon electrode modified by Au NSs with cubic structure, peak current was substantially received to 2.5 µA, which suggested that this film accelerate the electron transfer and electrochemical activity of the gold electrode. In addition to the Au NSs within the nanocomposite, the organic phase of aptamer strands was predominant. Consequently, the presence of oligonucleotide molecules can block the electron transfer at the interface between the electrolytes and electrode,

thereby leading to the increase of the peak current. Finally, the peak current was further reduce to 1.2 µA, when AU NSs with spherical structure were coated on GCE, which indicated the covering of RAC onto the electrode surface to further prevent the electron transfer.

Kinetic study

The scan rate effect on the electrochemical behavior of the different modified electrodes was studied in the presence of 0.01 M $[Fe(CN)_6]^{3-/4-}$. The scan rate was swept up between 2 to 1000 mV/s and their voltammograms have been illustrated in Fig. S6 (see supporting information shows the scan rate effect.

To display the effect of structure on the detection of RAC using aptasensors based on different developed strategies, Fig. S7 (see supporting information) shows the scan rate effect on the peak currents obtained from each step for the six modified electrodes. The results demonstrated that the peak currents value of the AU NSs-petal was the highest, thereby suggesting its relatively suitable electrochemical performances. Therefore, the Au NSs-CysA-GQDs-CS-GCE with the highest peak currents exhibited the most desirable aptasensing ability towards RAC detection. This observation can be explained with the homogeneous distribution of the Au NSs and high intensity of aptamer strands, which can improve the binding points with protein molecules. As shown in Fig. S7 (see supporting information), the surface coverage of the Au NSs with different structure/size coated on the GCE with relatively low electrochemical activity inhibits the access of electrons, leading to suitable electron-transfer efficiency of the system, which peak currents of the modified electrodes were increased.

The special surface coverage (I^*) of the Au Ns modified CysA-GQDs-CS-GCE was calculated using the study of the effect of the scan rate (V/s) on the oxidation peak current and the electrode

response. As presented in Fig. S7 (see supporting information), there is a linear relation between the oxidation peak of the electrode (A) and V/s at low scan rates indicating the electrocatalytic feature of the engineered system [32]. The value of the Γ^* were calculated as about 1.42×10^{-8} mol cm^{-2} using Eq. 1: [32]

$$Ip = \left(\frac{n^2F^2}{4RT}\right)\upsilon A\Gamma^* \quad (1)$$

where, I_p, n, F, R, T, υ, A and Γ^* are the oxidation peak current, total transferred electron, Faraday's constant (96486, $A.s.mol^{-1}$), gas constant (8.314, $JK^{-1}mol^{-1}$), temperature (298 K), potential sweep rate (V/s), total electrode surface (cm^2) and special surface (mol cm^{-2}) covered in different modification steps.

Analytical approach

To evaluate the analytical performance of the designed aptasensors, SWVs were recorded by adding different concentrations of RAC to the sensor to examine whether the peak currents could be used for quantification (Fig. 5). It demonstrates that the I_p values further decreases after the RAC detection, indicating that the binding of RAC with aptamer strands inhibits the access of electrons to the modified surface. The SWVs of different modified electrodes were conducted in 0.01 M $[Fe(CN)_6]^{3-/4-}$. Three samples exhibited the same trend: electrode materials presented a smaller current response. This difference in current response could be caused by that electrode materials blocked the electron transfer between the electrodes and solution. When RAC was assembled on the above aptamer-modified GCE, increase in the peak current was obtained. This confirmed successful interaction of RAC with APT modified interface.

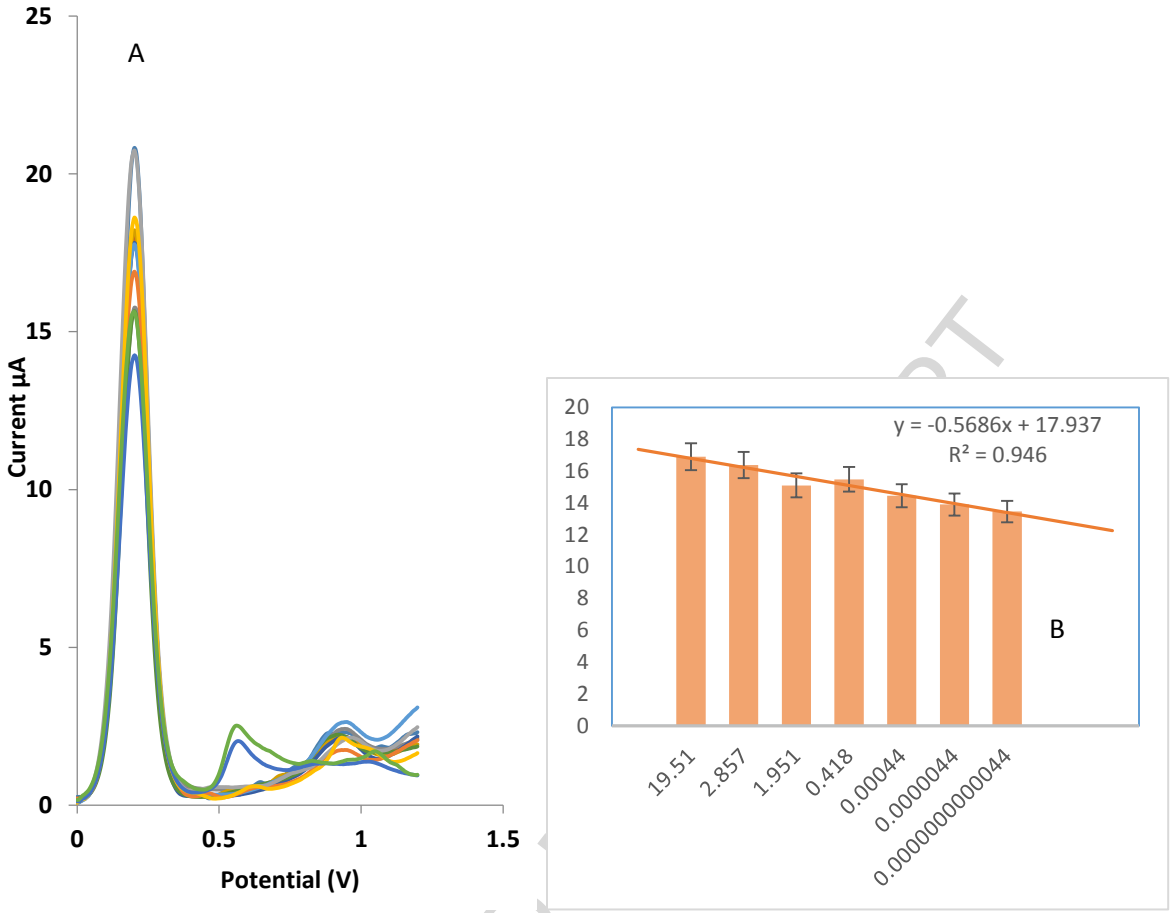

Fig. 5: **A**) DPVs of Apt-AuNSs- CysA-GQDs-CS-GCE in the presence of different concentration of RAC. **B**) Calibration curve

As shown in the Fig. 5B, the calibration plots displayed a good linear relationship in low concentration between the peak currents and RAC concentrations ranging from 19.51 µM-0.0044 fM. The lower limit of quantification (LLOQ) was 0.0044 fM. The same approach was used in the determination of the LLOQ for the detection RAC in unprocessed human plasma samples using proposed aptasensor. According to the obtained results, it was possible to apply this technique to the quantitative analysis of RAC in real samples using SWV techniques. For this purpose, 1 mL of unprocessed human plasma were taken and added into supporting electrolytes to reach a total

volume of 9 mL. Compared with the reported electrochemical methods listed in Table 1 for the RAC detection, the proposed aptasensors showed significant improvement in the detection of RAC. As can be seen, a lot of EC sensor methods for RAC have been reported and the representative method was shown in Table 1. Comparing with the published electrochemical methods in Table 1, advantages of the developed electrochemical apta-assays was apparent: (**I**) It could be seen that the detection limit of our aptasensor, is obviously better than other sensors. (**II**) About two orders of magnitude dynamic range in lower concentration level obtained in this study was wider than most reported electrochemical sensors and rivaled by only a few, with most only operating within 2-3 orders of magnitude of their level of detection. (**III**) The superior performance of the apta-assays over the reported methods highlighted the benefits that can be attributed to the novel preparation method of the apta-assays.

Table 1: Compartment the analytical parameters of some aptasensor for the detection of RAC

	Biosensor structure	**LOD**	**Dynamic range**	**Ref.**
Electrochemical Biosensor	Mesopores cellular foam (MCF) modified carbon paste electrode (MCF/CPE)	0.010 µM	0.050 - 3.0 µM	54
	Ordered mesoporous carbon modified electrode	0.060 µM	0.085 - 8.0 µM	55
	Carbon nanotube film-modified electrode	0.059 µM	0.15 - 5.9 µM	56
	Poly taurine/zirconia nanoparticles modified electrode	0.15 µM	1.0 – 28 µM	57
	Electrode modified with gold nanoparticles nanoparticles and multi-walled carbon nano tubes in a poly-arginine film on glassy carbon electrode	0.00010 µM	0.00010 -1.0 µM	58
	Carbon nanoparticle modified electrode	0.0020 µM	0.0020 -0.030 µM	59
	Flower-like gold nanostructure on ordered mesoporous carbon electrode	0.0044 µM	0.030 –75 µM	60
	disposable molecularly imprinted electrochemical sensor based on screen-printed electrode modified with ordered mesoporous carbon and gold nanoparticles nanoparticles	0.000042 µM	0.000050 - 0.0010 µM	61
	Glassy carbon electrodes modified with G/GNR composites	0.00051 µM	0.001- 2.7 µM	62
	AP-Ago (aptamer-agonists)-based gold electrode	1130 µM	0.000284-0.0284 µM	63
	AuNPs/GCE	0.0003 µM	0.001–10 µM	64
	Molecularly imprinted polymer film on gold electrode surface	0.0238 µM	0.2 - 1.4 µM	65

	molecularly imprinted quartz crystal microbalance (QCM) by electro depositing a poly-o-aminothiophenol membrane on an Au electrode surface modified by self-assembled Au nanoparticles(AuNPs)	1.17 μM	2.5-150 μM	66
	electro-polymerization of 4,5-dihydroxy-3-[(2-hydroxy-5-sulfophenyl)azo]-2,7-naphthalenedisulfonic acid trisodium salt (acid chrome blue K (ACBK))at a graphene oxide (GO)-nafion modified	0.0023 μM	0.0284-0.0512 μM	67
	Immobilizing complete antigen in agarose hydrogel films modified on a glassy carbon electrode	-	0.0284-2.84 μM	68
	silver–palladium alloynanoparticle-basedelectrochemicalbiosensor	0.00000432 μM	0.0000284-0.284 μM	69
	electrochemical immunosensor based on 3D Cu/Cu_2O@rGO nanocomposite	0.0000231 μM	0.000284- 0.0284 μM	70
	Electrochemical-Facial Deposition of MnO2 nanoflowers onto 3D RGO/Ni Foam templates	0.0116 μM	0.017 – 0.962 μM	71
	GO-modified GCE	0.0483 μM	0.0711-2.84 μM	72
	aptamer-bound AuNPs and graphene composite film	0.0000005 μM	0.000001 -0.01 μM	73
	label-free electrochemical immunosensor based on Au@Ag2S core@shell nanoparticles/magnetic chitosan/thionine matrix film (CSMCM)	0.00000711 μM	0.0284- 0.0000284 μM	74
	Screen-printed electrodes were modified with multi-wall carbon nanotubes (MWCNT) and molecularly imprinted membranes (MIM)			75
	electrochemical biosensor based on Mn3(PO4)2-like nanoflowers $Mn_3(PO4)_2$@RACanti $Mn_3(PO4)_2$@IgG $Mn_3(PO4)_2$@BSA@AuNPs	 0.0000265 μM 0.00001309 μM 0.000074 μM	0.0000284-2.84 μM	76
	aptamer based assay based on aggregation of gold nanoparticles in combination with a molecularly imprinted polymer	0.0284 μM	0.0284-1.138 μM	77
	electrochemical immunosensor based on chit-AuNPs	0.00000654 μM	0.00002484-0.0142 μM	78
	Apt-AuNSs-CysA-GQDs-CS-GCE	0.0044 fM	0.0044 fM - 19.55 μM	This work

Stability and repeatability of the developed aptasensors

The reusability of the aptasensor is considerably important for practical application, such as clinical diagnoses and biological monitoring, which is dependent on the stability and regeneration ability of the aptasensor. In the present work, when the fabricated aptasensor was stored at 4 °C for one week and subsequently measured by DPV, the change in the peak currents response was only 3.7% compared with the initial test, which indicated the good stability of the aptasensor.

Analysis of real plasma samples

To examine the potential practical applications of the apta-sensor, different concentrations of RAC were spiked into human plasma samples (Fig. S8 (see supporting information). The human plasma samples were not processed and treated. Then, the calibration curve was obtained.

4. Conclusions

In summary, biopolymer nanocomposites of CS-GQDs were prepared by a simple assembly strategy using CS as the matrix and GQDs. Well-dispersed status of GQDs within CS was achieved via electrostatic attraction and H-bondings between CS and GQDs. Variety of shapes of gold nanostructures with different sizes from zero-dimensional nanoparticles to spherical structures were prepared by one-step template-assistant green electrodeposition method. Fully electrochemical methodology was used to prepare a new transducer on a GCE surface which provided a high surface area to immobilize a high amount of the aptamer. Therefore, a label free electrochemical (EC) aptasensor for ultrasensitive detection of ractopamine (RAC) was developed. A special immobilization media consisting of Au NSs /CysA GQDs-CSA was utilized to improve conductivity and performance of the biosensor. The RAC aptamer was attached on Au NSs of the composite membrane via Au-S bond. The results show that Apt, Au NSs/CysA GQDs-CSA exhibited good biocompatibility, and acceptable specificity for RAC detection; thus, the related fabricated electrochemical aptasensors exhibited considerably low limit of quantification 0.0044 fM. Also, under the optimized experimental conditions, the proposed aptasensor of exhibited excellent analytical performance for determination of RAC in human biofluids, ranging from 0.0044 fM to 19.55 µM with a low limit of quantification of 0.0044 fM. The results indicated that the presence of Au NSs and GQDs-CS-CysA can improve the affinity of the RAC binding.

Acknowledgement

The authors would like to acknowledge the financial supports from Tabriz University of Medical Sciences, Tabriz, Iran. This study was supported by Tabriz University of Medical Science as MSc thesis of Arezoo Mirzaie.

5. References

1. C. Crescenzi , S. Bayoudh S, P. Cormack, T. Klein, K. Ensing. Determination of clenbuterol in bovine liver by combining matrix solid-phase dispersion and molecularly imprinted solid-phase extraction followed by liquid chromatography/electrospray ion trap multiple-stage mass spectrometry. *Anal. Chem.* **73(10)**, 2001, 2171-7.
2. Shishani EI, Chai SC, Jamokha S, Aznar G, Hoffman MK. Determination of ractopamine in animal tissues by liquid chromatography-fluorescence and liquid chromatography/tandem mass spectrometry. Analytica Chimica Acta. 2003;483(1-2):137-45.
3. Brambilla G, Cenci T, Franconi F, Galarini R, Macrı A, Rondoni F, Clinical and pharmacological profile in a clenbuterol epidemic poisoning of contaminated beef meat in Italy. Toxicology letters. 2000;114(1-3):47-53.
4. Smith D. Total radioactive residues and clenbuterol residues in swine after dietary administration of [14C] clenbuterol for seven days and preslaughter withdrawal periods of zero, three, or seven days. Journal of animal science. 2000;78(11):2903-12.

5. Duan J, He D, Wang W, Liu Y, Wu H, Wang Y, Glassy carbon electrode modified with gold nanoparticles for ractopamine and metaproterenol sensing. Chemical Physics Letters. 2013;574:83-8.
6. Blanca J, Muñoz P, Morgado M, Méndez N, Aranda A, Reuvers T, et al. Determination of clenbuterol, ractopamine and zilpaterol in liver and urine by liquid chromatography tandem mass spectrometry. Analytica Chimica Acta. 2005;529(1-2):199-205.
7. Wang S, Wei J, Hao T, Guo Z. Determination of ractopamine in pork by using electrochemiluminescence inhibition method combined with molecularly imprinted stir bar sorptive extraction. Journal of Electroanalytical Chemistry. 2012;664:146-51.
8. He L, Su Y, Zeng Z, Liu Y, Huang X. Determination of ractopamine and clenbuterol in feeds by gas chromatography-mass spectrometry. Animal Feed Science and Technology. 2007;132(3-4):316-23.
9. Jiang X, Zhu Z, Sun Z, Wang L, Zhou L, Miao H, et al. The development of an indirect competitive immunomagnetic-proximity ligation assay for small-molecule detection. Analyst. 2013;138(2):438-42.
10. Zheng S, Song S, Lan H, Qu G, Li R, Wu A, et al. Newly combined method of molecularly imprinted solid-phase extraction with ELISA for rapid detection of clenbuterol in animal-tissue samples. Analytical Letters. 2009;42(3):600-14.
11. Tahernejad-Javazmi F, Shabani-Nooshabadi M, Karimi-Maleh H. Analysis of glutathione in the presence of acetaminophen and tyrosine via an amplified electrode with MgO/SWCNTs as a sensor in the hemolyzed erythrocyte. Talanta. 2018;176:208-13.
12. Cheraghi S, Taher MA, Karimi-Maleh H. A sensitive amplified sensor based on improved carbon paste electrode with 1-methyl-3-octylimidazolium tetrafluoroborate and

ZnO/CNTs nanocomposite for differential pulse voltammetric analysis of raloxifene. Applied Surface Science. 2017;420:882-5.

13. Cheraghi S, Taher MA, Karimi-Maleh H, Faghih-Mirzaei E. A nanostructure label-free DNA biosensor for ciprofloxacin analysis as a chemotherapeutic agent: an experimental and theoretical investigation. New Journal of Chemistry. 2017;41(12):4985-9.
14. Cheraghi S, Taher MA, Karimi-Maleh H. Highly sensitive square wave voltammetric sensor employing CdO/SWCNTs and room temperature ionic liquid for analysis of vanillin and folic acid in food samples. Journal of Food Composition and Analysis. 2017;62:254-9.
15. Karimi-Maleh H, Shojaei AF, Tabatabaeian K, Karimi F, Shakeri S, Moradi R. Simultaneous determination of 6-mercaptopruine, 6-thioguanine and dasatinib as three important anticancer drugs using nanostructure voltammetric sensor employing Pt/MWCNTs and 1-butyl-3-methylimidazolium hexafluoro phosphate. Biosensors and Bioelectronics. 2016;86:879-84.
16. Malekzad H, Hasanzadeh M, Shadjou N, Jouyban A. Highly sensitive immunosensing of prostate specific antigen using poly cysteine caped by graphene quantum dots and gold nanoparticle: a novel signal amplification strategy. International journal of biological macromolecules. 2017;105:522-32.
17. Xiao J, Qi L. Surfactant-assisted, shape-controlled synthesis of gold nanocrystals. Nanoscale. 2011;3(4):1383-96.
18. Lord H, Kelley SO. Nanomaterials for ultrasensitive electrochemical nucleic acids biosensing. Journal of Materials Chemistry. 2009;19(20):3127-34.

19. Soleymani L, Fang Z, Sargent EH, Kelley SO. Programming the detection limits of biosensors through controlled nanostructuring. Nature Nanotechnology. 2009;4(12):844.

20. Hasanzadeh M, Mokhtarzadeh A, Shadjou N, Mahboob S. An innovative immunosensor for detection of tumor suppressor protein p53 in unprocessed human plasma and cancer cell lysates. International journal of biological macromolecules. 2017;105:1337-48.

21. X. Zhang, W. Hu, J. Li, L. Tao, Y. Wei. A comparative study of cellular uptake and cytotoxicity of multi-walled carbon nanotubes, graphene oxide, and nanodiamond. ***Toxicol. Res.***, 2012,**1**, 62-68

22. X. Zhang, K. Wang, M. Liu, X. Zhang, L. Tao, Y. Chen, Y. Wei. Polymeric AIE-based nanoprobes for biomedical applications: recent advances and perspectives. *Nanoscale,* 2015,7, 11486-11508.

23. X. Zhang, S. Wang, L. Xu, L. Feng, Y. Ji, L. Tao, S. Li, Y. Wei. Biocompatible polydopamine fluorescent organic nanoparticles: facile preparation and cell imaging. *Nanoscale*, 2012,4, 5581-5584.

24. Shi Y, Xu D, Liu M, Fu L,Wan Q, Mao L, Dai Y, Wen Y, Zhang X, Wei Y. Room temperature preparation of fluorescent starch nanoparticles from starch-dopamine conjugates and their biological applications. *Mater Sci Eng C* 2018;82:204-209.

25. Jiang R, Liu H, Liu M, Tian J, Huang Q, Huang H, Wen Y, Cao QY, Zhang X, Wei Y. A facile one-pot Mannich reaction for the construction of fluorescent polymeric nanoparticles with aggregation-induced emission feature and their biological imaging. *Mater Sci Eng C* 2017 81:416-421.

26. Wei D, Xue Y, Huang H, Liu M, Zeng G, Wan Q, Liu L, Yu J, Zhang X, Wei Y. Fabrication, self-assembly and biomedical applications of luminescent sodium hyaluronate with aggregation-induced emission feature. *Mater Sci Eng C* 2017;81:120-126.
27. Jiang R, Liu M, Li C, Huang Q, Huang H, Wan Q, Wen Y, Cao QY, Zhang X, Wei Y. Facile fabrication of luminescent polymeric nanoparticles containing dynamic linkages via a one-pot multicomponent reaction: Synthesis, aggregation-induced emission and biological imaging. *Mater Sci Eng C* 2017;80:708-714.
28. Xu D, Liu M, Zou H, Tian J, Huang H, Wan Q, Dai Y, Wen Y, Zhang X, Wei Y. A new strategy for fabrication of water dispersible and biodegradable fluorescent organic nanoparticles with AIE and ESIPT characteristics and their utilization for bioimaging. *Talanta*. 2017;174:803-808.
29. Mao L, Liu M, Jiang R, Huang Q, Dai Y, Tian J, Shi Y, Wen Y, Zhang X, Wei Y. The one-step acetalization reaction for construction of hyperbranched and biodegradable luminescent polymeric nanoparticles with aggregation-induced emission feature. *Mater Sci Eng C* 2017 1;80:543-548.
30. Liu Y, Mao L, Liu X, Liu M, Xu D, Jiang R, Deng F, Li Y, Zhang X, Wei Y. A facile strategy for fabrication of aggregation-induced emission (AIE) active fluorescent polymeric nanoparticles (FPNs) via post modification of synthetic polymers and their cell imaging. *Mater Sci Eng C* 2017;79:590-595.
31. Shi Y, Jiang R, Liu M, Fu L, Zeng G, Wan Q, Mao L, Deng F, Zhang X, Wei Y. Facile synthesis of polymeric fluorescent organic nanoparticles based on the self-polymerization of dopamine for biological imaging. *Mater Sci Eng C* 2017;77:972-977.

32. Hasanzadeh M, Shadjou N, Marandi M. Graphene quantum dots functionalized by chitosan and β-cyclodextrin: an advanced nanocomposite for sensing of multi-analytes at physiological pH. J. Nanosci. Nanotech. 17 (7), 2017, 4598-4607.

33. Gambhire MN, Ambade KW, Kurmi SD, Kadam VJ, Jadhav KR. Development and in vitro evaluation of an oral floating matrix tablet formulation of diltiazem hydrochloride. AAPS PharmSciTech. 2007;8(3):E166-E74.

34. Argüelles-Monal W, Hechavarria O, Rodriguez L, Peniche C. Swelling of membranes from the polyelectrolyte complex between chitosan and carboxymethyl cellulose. Polymer Bulletin. 1993;31(4):471-8

35. Sun H ,Wu L, Wei W, Qu X. Recent advances in graphene quantum dots for sensing. Materials Today. 2013;16(11):433-42.

36. Konwar A, Gogoi N, Majumdar G, Chowdhury D. Green chitosan–carbon dots nanocomposite hydrogel film with superior properties. Carbohydrate polymers. 2015;115:238-45.

37. Zangmeister RA, Park JJ, Rubloff GW, Tarlov MJ. Electrochemical study of chitosan films deposited from solution at reducing potentials. Electrochimica acta. 2006;51(25):5324-33.

38. Stoilova O, Koseva N, Manolova N, Rashkov I. Polyelectrolyte complex between chitosan and poly (2-acryloylamido-2-methylpropanesulfonic acid). Polymer Bulletin. 1999;43(1):67-73.

39. Shi L, Chu Z, Liu Y, Jin W, Chen X. Facile synthesis of hierarchically aloe-like gold micro/nanostructures for ultrasensitive DNA recognition. Biosensors and Bioelectronics. 2013;49:184-91.

40. Hoefling M, Iori F, Corni S, Gottschalk K-E. Interaction of amino acids with the Au (111) surface: adsorption free energies from molecular dynamics simulations. Langmuir. 2010;26(11):8347-51.

41. Ramezani F, Amanlou M, Rafii-Tabar H. Comparison of amino acids interaction with gold nanoparticle. Amino acids. 2014;46(4):911-20.

42. Crespilho FN, Lima FC, da Silva AB, Oliveira Jr ON, Zucolotto V. The origin of the molecular interaction between amino acids and gold nanoparticles: A theoretical and experimental investigation. Chemical Physics Letters. 2009;469(1-3):186-90.

43. Feng J, Pandey RB, Berry RJ, Farmer BL, Naik RR, Heinz H. Adsorption mechanism of single amino acid and surfactant molecules to Au {111} surfaces in aqueous solution: design rules for metal-binding molecules. Soft Matter. 2011;7(5):2113-20.

44. Sethi M, Knecht MR. Experimental studies on the interactions between Au nanoparticles and amino acids: bio-based formation of branched linear chains. ACS applied materials & interfaces. 2009;1(6):1270-8.

45. Joshi H, Shirude PS, Bansal V, Ganesh K, Sastry M. Isothermal titration calorimetry studies on the binding of amino acids to gold nanoparticles. The Journal of Physical Chemistry B. 2004;108(31):11535-40.

46. Maruyama T, Fujimoto Y, Maekawa T. Synthesis of gold nanoparticles using various amino acids. Journal of colloid and interface science. 2015;447:254-7.

47. Wright LB, Merrill NA, Knecht MR, Walsh TR. Structure of arginine overlayers at the aqueous gold interface: Implications for nanoparticle assembly. ACS applied materials & interfaces. 2014;6(13):10524-33.

48. Lv Z-Y, Li A-Q, Fei Y, Li Z, Chen J-R, Wang A-J, Facile and controlled electrochemical route to three-dimensional hierarchical dendritic gold nanostructures. Electrochimica Acta. 2013;109:136-44.

49. Malekzad H, Jouyban A, Hasanzadeh M, Shadjou N, de la Guardia M. Ensuring food safety using aptamer based assays: Electroanalytical approach. Trends in Analytical Chemistry. 2017;94:77-94.

50. Hasanzadeh M, Shadjou N, de la Guardia M. Aptamer-based assay of biomolecules: Recent advances in electro-analytical approach. Trends in Analytical Chemistry. 2017, 119.

51. Omidinia E, Shadjou N, Hasanzadeh M. Aptamer-based biosensor for detection of phenylalanine at physiological pH. Applied biochemistry and biotechnology. 2014;172(4):2070-80.

52. Xie L, Ya Y, Wei L. Mesopores cellular foam-based electrochemical sensor for sensitive determination of ractopamine. Int J Electrochem Sci. 2017;12:9714-24.

53. Yang X, Feng B, Yang P, Ding Y, Chen Y, Fei J. Electrochemical determination of toxic ractopamine at an ordered mesoporous carbon modified electrode. Food chemistry. 2014;145:619-24.

54. Liu Z, Zhou Y, Wang Y, Cheng Q, Wu K. Enhanced oxidation and detection of toxic ractopamine using carbon nanotube film-modified electrode. Electrochimica Acta. 2012;74:139-44.

55. Rajkumar M, Li Y-S, Chen S-M. Electrochemical detection of toxic ractopamine and salbutamol in pig meat and human urine samples by using poly taurine/zirconia nanoparticles modified electrodes. Colloids and Surfaces B: Biointerfaces. 2013;110:242-7.

56. Zhou Y, Wang P, Su X, Zhao H, He Y. Sensitive immunoassay for the β-agonist ractopamine based on glassy carbon electrode modified with gold nanoparticles and multi-walled carbon nanotubes in a film of poly-arginine. Microchimica Acta. 2014;181(15-16):1973-9.

57. Yao S, Hu Y, Li G, Zhang Y. Adsorption behavior of ractopamine on carbon nanoparticle modified electrode and its analytical application. Electrochimica Acta. 2012;77:83-8.

58. Wei Q, Wang Q, Wang H, Gu H, Zhang Q, Gao X, Formation of flowerlike gold nanostructure on ordered mesoporous carbon electrode and its application in electrochemical determination of ractopamine. Materials Letters. 2015;147:58-60.

59. Ma M, Zhu P, Pi F, Ji J, Sun X. A disposable molecularly imprinted electrochemical sensor based on screen-printed electrode modified with ordered mesoporous carbon and gold nanoparticles for determination of ractopamine. Journal of Electroanalytical Chemistry. 2016;775:171-8.

60. Bai W, Huang H, Li Y, Zhang H, Liang B, Guo R, Direct preparation of well-dispersed graphene/gold nanorod composites and their application in electrochemical sensors for determination of ractopamine. Electrochimica Acta. 2014;117:322-8.

61. Chen D, Yang M, Zheng N, Xie N, Liu D, Xie C, A novel aptasensor for electrochemical detection of ractopamine, clenbuterol, salbutamol, phenylethanolamine and procaterol. Biosensors and Bioelectronics. 2016;80:525-31.

62. Kong L-J, Pan M-F, Fang G-Z, Qian K, Wang S. An electrochemical sensor for rapid determination of ractopamine based on a molecularly imprinted electrosynthesized o-aminothiophenol film. Analytical and bioanalytical chemistry. 2012;404(6-7):1653-60.

63. Kong L-J, Pan M-F, Fang G-Z, He X-l, Yang Y-k, Dai J, Molecularly imprinted quartz crystal microbalance sensor based on poly (o-aminothiophenol) membrane and Au nanoparticles for ractopamine determination. Biosensors and Bioelectronics. 2014;51:286-92.

64. Duan J, He D, Wang W, Liu Y, Wu H, Wang Y, Glassy carbon electrode modified with gold nanoparticles for ractopamine and metaproterenol sensing. Chemical Physics Letters. 2013;574:83-8.

65. Lin X, Ni Y, Kokot S. A novel electrochemical sensor for the analysis of β-agonists: the poly (acid chrome blue K)/graphene oxide-nafion/glassy carbon electrode. Journal of hazardous materials. 2013;260:508-17.

66. Shen L, He P. An electrochemical immunosensor based on agarose hydrogel films for rapid determination of ractopamine. Electrochemistry Communications. 2007;9(4):657-6.2

67. Wang H, Zhang Y, Li H, Du B, Ma H, Wu D, A silver-palladium alloy nanoparticle-based electrochemical biosensor for simultaneous detection of ractopamine, clenbuterol and salbutamol. Biosensors and Bioelectronics. 2013;49:14-9.

68. Wang M, Kang M, Guo C, Fang S, He L, Jia C, Electrochemical biosensor based on Cu/Cu_2O nanocrystals and reduced graphene oxide nanocomposite for sensitively detecting ractopamine. Electrochimica Acta. 2015;182:668-75.

69. Wang MY, Zhu W, Ma L, Ma JJ, Zhang DE, Tong ZW, Enhanced simultaneous detection of ractopamine and salbutamol–Via electrochemical-facial deposition of MnO_2 nanoflowers onto 3D RGO/Ni foam templates. Biosensors and Bioelectronics. 2016;78:259-66.

70. Wu C, Sun D, Li Q, Wu K. Electrochemical sensor for toxic ractopamine and clenbuterol based on the enhancement effect of graphene oxide. Sensors and Actuators B: Chemical. 2012;168:178-84.

71. Yang F, Wang P, Wang R, Zhou Y, Su X, He Y, Label free electrochemical aptasensor for ultrasensitive detection of ractopamine. Biosensors and Bioelectronics. 2016;77:347-52.

72. Zhang Y, Ma H, Wu D, Li Y, Du B, Wei Q. Label-free immunosensor based on Au@Ag_2S nanoparticles/magnetic chitosan matrix for sensitive determination of ractopamine. Journal of Electroanalytical Chemistry. 2015;741:14-9.

73. Zhang H, Liu G, Chai C. A novel amperometric sensor based on screen-printed electrode modified with multi-walled carbon nanotubes and molecularly imprinted membrane for rapid determination of ractopamine in pig urine. Sensors and Actuators B: Chemical. 2012;168:103-10.

74. Zhang Z, Zhang Y, Song R, Wang M, Yan F, He L, Manganese (II) phosphate nanoflowers as electrochemical biosensors for the high-sensitivity detection of ractopamine. Sensors and Actuators B: Chemical. 2015;211:310-7.

75. Wang P, Su X, Shi L, Yuan Y. An aptamer based assay for the β-adrenergic agonist ractopamine based on aggregation of gold nanoparticles in combination with a molecularly imprinted polymer. Microchimica Acta 183, 2016, 905.

76. He L, Guo C, Song Y, Zhang S, Wang M, Peng D, Chitosan stabilized gold nanoparticle based electrochemical ractopamine immunoassay. Microchimica Acta. 2017;184(8):2919-24.